

1 Imaging of Atmospheric Gravity Waves in the
2 Stratosphere and Upper Mesosphere using Satellite
3 and Ground-Based Observations Over Australia
4 During the TWPICE Campaign

J. H. Hecht,¹ M. J. Alexander,² R. L. Walterscheid,¹ L. J. Gelinas,¹ R. A.

Vincent,³ A. D. MacKinnon,³ J. M. Woithe,³ P. T. May,⁴ W. R. Skinner,⁵

M.G. Mlynczak,⁶ and J. M. Russell III⁷

¹Space Sciences Department, The Aerospace Corporation, Los Angeles, California, USA.

²NWRA/CoRA Division, Boulder, Colorado, USA.

³Department of Physics and Mathematical Physics, University of Adelaide, Adelaide, South Australia, Australia.

⁴Centre for Australian Weather and Climate Research: A Partnership between the Australian Bureau of Meteorology and CSIRO, Melbourne, Australia.

⁵Department of Atmospheric, Oceanic and Space Sciences University of Michigan Ann Arbor, Michigan, USA.

⁶NASA Langley Research Center, Hampton, Virginia, USA.

⁷Center for Atmospheric Sciences, Hampton University, Hampton, Virginia, USA.

5 **Abstract.** During the Tropical Warm Pool International Cloud Exper-
6 iment (TWPICE) an intense tropical low was situated between Darwin and
7 Alice Springs Australia. Observations made on 31 January 2006 by the At-
8 mospheric Infrared Sounder instrument on the NASA Aqua satellite imaged
9 the presence of atmospheric gravity waves, at approximately 40 km altitude,
10 with horizontal wavelengths between 200 and 400 km that were originating
11 from the region of the storm. Airglow images obtained from Alice Springs
12 (about 600 km from the center of the low) showed the presence of similar
13 waves with observed periods of 1 to 2 hours. The images also revealed the
14 presence of 30 to 45 km horizontal wavelength AGWs with shorter observed
15 periods of near 15 to 25 minutes. Ray tracing calculations show that (a) some
16 of the long wavelength waves travelled on rays, without ducting, to the al-
17 titudes where the observations were obtained, and (b) shorter period waves
18 rapidly reached 85 km altitude at a horizontal distance close to the storm,
19 thus occurring over Alice Springs only if they were trapped or ducted. The
20 mesospheric inversion layer seen in the measured temperature data almost
21 forms such a trapped region. The winds, therefore, critically control the for-
22 mation of the trapped region. Wind profiles deduced from the available data
23 show the plausibility for the formation of such a trapped region. Variations
24 in the wind however would make ideal trapped region conditions short lived
25 and this may account for the sporadic nature of the short-period wave ob-
26 servations.

1. Introduction

27 Although atmospheric gravity waves (AGWs) have been imaged in the airglow for over
28 30 years [*Hecht, 2004a*] their sources have not been fully determined. While convection
29 in the troposphere is likely a major source especially in the tropics [*Fritts and Alexan-*
30 *der, 2003*], the nature of the AGWs they produce and how they reach the 80 to 100 km
31 altitudes where airglow originates are still uncertain. It has been particularly difficult
32 for ground-based imaging techniques to study this problem. First, short horizontal wave-
33 length AGWs, often seen in images, typically reach the airglow region only a few hundred
34 km from their source which means that ground-based imagers need to be placed close
35 to the source region. But periods of intense convective activity are also periods of con-
36 siderable cloudiness which often precludes imaging observations. Second, there is some
37 evidence that the AGWs seen in imagers may be ducted a considerable horizontal distance
38 from their source making it difficult to determine the origin of those waves (e.g. [*Walter-*
39 *scheid et al., 1999*]). Third, until recently there were almost no space-based instruments
40 capable of imaging AGWs above the troposphere. Nevertheless, there have been several
41 studies which attempted to determine a specific AGW source. They fall into two classes,
42 (1) those that consider AGWs which travel directly from the convective source to the
43 observation altitude, and (2) those which consider the ducting or trapping of AGWs.

44 In the first category there are to our knowledge only a few such reports. The first was
45 a ground-based study by *Taylor and Hapgood* [1988]. They observed curved wave fronts
46 which they determined had a center about 200 to 500 km from the observed wavefronts.
47 They used estimates of the wind and temperature profiles from the limited satellite and

48 model data then available for their analysis. The observed horizontal wavelength, λ_h ,
49 was about 25 km, and the intrinsic period was found to be about 17 minutes. They
50 concluded that the AGWs took about 6 hours to reach airglow altitudes and winds were
51 found to steer the wave packets about 200 km to the west. From meteorological charts
52 and lightning data they showed that there were transient thunderstorms present in the
53 right region to be the source of these AGWs.

54 A second study was based on space-based observations by *Dewan et al.* [1998]. They
55 used infrared data observed by the Midcourse Space Experiment (MSX) satellite and
56 originating near 40 km altitude which showed circular wavefronts whose λ_h was about 25
57 km. They followed the analysis procedures used by *Taylor and Hapgood* [1988]. However,
58 since they did not have time resolution, they could only place reasonable limits on the
59 frequency and other derived parameters. For comparison with *Taylor and Hapgood* [1988]
60 their intrinsic period was estimated at about 10 minutes. However, their analysis was
61 convincing that the source was a transient thunderstorm. since their observations were
62 from 40 km where the wind and temperature variability are typically much less than at
63 higher altitudes where large amplitude tides and AGWs exist and measured variability is
64 large [*Larsen, 2002*].

65 A third study was by *Sentman et al.* [2003] who were observing sprites over convective
66 sources. Their viewing geometry allowed them to observe AGWs over thunderstorms and
67 their airglow images showed nearly concentric wavefronts emanating from a tropospheric
68 source region. Their analysis, which because they had no winds assumed that the observed
69 period was the intrinsic period, showed λ_h values between 40 and 50 km with periods near

70 10 minutes. This study is quite impressive in that the link between the convective source
71 and the AGW observations appears well established.

72 In the second category there are a number of studies that attempt to explain the preva-
73 lence of AGWs in airglow imagers with λ_h values that are typically a few tens of kilometers,
74 have ground-based periods of ten to a few tens of minutes, and are imaged a great distance
75 away from a specific convective source, (e.g. [Nakamura *et al.*, 1999; Walterscheid *et al.*,
76 1999; Hecht *et al.*, 2001; Ejiri *et al.*, 2003; Nakamura *et al.*, 2003; Hecht *et al.*, 2004b;
77 Suzuki *et al.*, 2004; Pautet *et al.*, 2005]). Walterscheid *et al.* [1999] advanced the idea that
78 this was due to ducting of the AGWs in a thermal duct present in the upper mesosphere
79 and lower thermosphere. Hecht *et al.* [2001] later suggested that modifications of this
80 thermal duct by winds need also be considered and that the waves may be trapped rather
81 than purely ducted. A specific example of such horizontal propagation through such a
82 trapped region was the study performed using observations obtained during the Darwin
83 Area Wave Experiment (DAWEX) [Hecht *et al.*, 2004b] which occurred from October to
84 December 2001. [Hecht *et al.*, 2004b] modelled the propagation of AGWs produced by in-
85 tense convective activity at Darwin(12.5°S, 130.8°E), Australia to the observation region
86 in the airglow over Alice Springs (23.8°S, 133.9°E) about 1290 km to the south.

87 Finally, also in the second category, Vadas *et al.* [2008] used ray tracing techniques to
88 identify the source of medium-scale AGWs in Brazil with λ_h values up to 160 km. They
89 provide convincing evidence that the source is convection. However, in some cases the
90 AGWs would reach the airglow altitude region close to the source, and thus additional
91 horizontal transport of the wave packets, presumably via trapping or ducting, would be
92 required for the AGWs to reach the atmosphere above the observing site. Modelled

93 temperature profiles are used for this analysis. This study also provides a quantitative
94 analysis of the energy available in the convective source, as parameterized by the measured
95 Convective Available Potential Energy (CAPE) and they show that it is sufficient to excite
96 the observed AGWs.

97 Both categories of observations suggest that in these cases short-period, short-horizontal
98 wavelength AGWs are produced by convective activity. This seems to be in line with
99 a number of studies that indicate such waves should be produced by these storms
100 (e.g.[*Walterscheid et al.*, 2001; *Alexander et al.*, 2004; *Vadas and Fritts*, 2006]). How-
101 ever, these studies also indicate that AGWs with somewhat longer wavelengths (up to a
102 few hundred kilometers) may also be produced. Furthermore, *Walterscheid et al.* [2001]
103 suggest that acoustic waves with periods of a few minutes may also be present in the
104 region above the storm.

105 The studies cited above provide data on AGWs which are produced by convective activ-
106 ity and which propagate into the stratosphere and mesosphere. However, our knowledge
107 of these two classes of events is far from complete. First, except for the category one
108 *Sentman et al.* [2003] study the identification of specific sources is only tentative. None
109 of the category one studies had realistic winds and temperatures to constrain a ray trace.
110 In the DAWEX study the source was sufficiently removed from the observations that the
111 AGWs could only reach Alice Springs via trapping or ducting; hence the specific source
112 region was uncertain. Second, all the studies cited were most sensitive to, and only re-
113 ported on, short λ_h , or in one case [*Vadas et al.*, 2008] medium λ_h AGWs, and thus the
114 presence or absence of larger scale waves is unknown. Third, all the studies focussed on
115 AGWs produced by transient events. None observed airglow emissions during a large

116 storm. Observations during such an event would allow a determination of whether these
117 storms also produce AGWs that have horizontal wavelengths restricted to below 160 km.

118 The Tropical Warm Pool International Cloud Experiment (TWPICE) which took place
119 during the first two months of 2006 near Darwin was organized to study convective storm
120 activity in the troposphere [May *et al.*, 2008]. Two of the deployed instruments, a meteor
121 radar at Darwin and an airglow imager at Alice Springs, were used for observations of
122 wave activity in the 80 to 100 km region. During TWPICE a very intense tropical low
123 developed in the region between Darwin and Alice Springs. The low was nearly stationary
124 for several days and developed into a tropical cyclone like storm. During some of this
125 period the skies were clear over Alice Springs and in particular, on 31 January 2006,
126 ground-based observations showed frequent small λ_h AGWs in the Alice Springs airglow
127 imager. As described in a later section these data also allowed observations of AGWs
128 whose λ_h are larger than the instrument field of view of about 100 kilometers at airglow
129 altitudes (e.g. [Hecht *et al.*, 1997]).

130 In addition to these ground-based observations there were overpasses of the NASA Ther-
131 mosphere Ionosphere Mesosphere Energetics and Dynamics (TIMED) and Aqua satellites.
132 Data from the TIMED Doppler Interferometer (TIDI) instrument [Killeen *et al.*, 1999;
133 Skinner *et al.*, 2003; Niciejewski *et al.*, 2003] when combined with the Darwin meteor
134 radar [Holdsworth *et al.*, 2004] and Buckland Park (34.9°S, 138.6°E) Medium Frequency
135 (MF) radar [Holdsworth *et al.*, 2004] allowed an estimate of the wind fields in the upper
136 mesosphere. These fields could be extended down to the ground using the European Cen-
137 ter for Medium-Range Weather Forecasts (ECMWF) assimilation and Horizontal Wind
138 Model (HWM) [Hedin *et al.*, 1996] data. The TIMED Sounding of the Atmosphere using

139 Broadband Emission Radiometry (SABER) instrument [*Russell et al.*, 1999] allowed tem-
140 peratures to be determined from the troposphere to above 100 km altitude. Data from
141 the Atmospheric Infrared Sounder (AIRS) instrument [*Aumann et al.*, 2003] on the NASA
142 Aqua satellite are used to image AGWs at approximately 40 km altitude (e.g. [*Alexander*
143 *and Barnet*, 2007; *Alexander and Teitelbaum*, 2007])). This paper reports on these data
144 that provide a means to study AGWs in the upper atmosphere that are generated by this
145 intense tropical storm system.

2. Experimental Instrumentation and Technique

146 This work uses a number of different ground-based, satellite-based, and model/assimilation
147 techniques. To guide the reader Figure 1 shows their locations, where applicable. Table
148 1 lists their main attributes and which parameters they address.

2.1. Data and Models

2.1.1. Airglow Imagers

150 The airglow instrument at Alice Springs (AS) is a modified version of the Aerospace
151 charge coupled device (CCD) nightglow camera which was originally described by *Hecht*
152 *et al.* [1994] and further described in *Hecht et al.* [2004b]. The imager now uses a 1536
153 by 1024 Kodak CCD chip. The pixels are binned 8 x 8, resulting in images that have 192
154 x 128 pixels. The angular field of view is now 46° by 69° giving a spatial field of view
155 of approximately 75 x 122 km at 90 km altitude. This instrument obtains images of the
156 OH Meinel (6,2) (hereinafter OHM) and O2 Atmospheric (0,1) band (hereinafter O2A)
157 band emissions. A sequence of five images is obtained, each at 1 min integration, through
158 separate narrow passband filters. Two of the filters cover two different rotational lines of

159 OHM, two filters cover different portions of O2A, and one filter covers the background
160 and has almost no airglow emission in its passband. The latter is used to correct the
161 airglow images for background skylight. Thus, one can obtain images of the OHM and
162 O2A airglow, the intensity and temperature of the OHM and O2A emissions, and AGW
163 horizontal wavelengths and ground-based phase velocities, e.g. [Hecht *et al.*, 1997, 2001].
164 The focus in this work is on AGWs so the main discussion will be on OHM image data
165 where the signal to noise is greater.

166 **2.1.2. AIRS instrument on the NASA Aqua satellite**

167 The NASA Aqua satellite was launched in 2002. One of the instruments on board
168 is the Atmospheric Infrared Sounder (AIRS) [Aumann *et al.*, 2003] that measures IR
169 radiance from many channels including several from the CO₂ 15 micron band used in
170 this study. Several of these channels sample high stratospheric altitudes (approximately
171 40 km) with a vertical weighting function width of about 12 km. These high altitude
172 channels are insensitive to the influence of tropospheric clouds but would be sensitive
173 to AGWs with vertical wavelengths much above 12 km. The AIRS footprint at nadir
174 is 13.5 km and the image swath is about 1630 km wide. For the high altitude channels
175 the noise levels are low enough (a few tenths of a degree) so that waves with brightness
176 temperature amplitudes of 1K can be seen (e. g. [Alexander and Barnett, 2007; Alexander
177 and Teitelbaum, 2007]). The relationship between the measured radiance and derived
178 brightness temperature perturbations is given by equation 5 in Alexander and Barnett
179 [2007]. The techniques used to extract AGW amplitudes and wavelengths from these data
180 are wavelet-based and are described in detail in Alexander and Barnett [2007]. A main
181 focus of this paper is the observation over central Australia that occurred at approximately

182 1623 Universal Time (UT) on 31 January 2006. This swath is shown in orange in Figure
183 1.

184 **2.1.3. Meteor radar at Darwin**

185 As part of the TWPICE campaign a meteor wind measuring radar was located near
186 Darwin. It was an all-sky system similar to that described by *Holdsworth et al.* [2004]. A
187 single crossed-dipole antenna was used for transmission and five crossed-dipole antennas
188 arranged in a cross configuration were used for reception. Using a 7.5 kW peak power
189 transmitter about 15,000 meteors were observed each day during TWPICE. This system
190 provided hourly average zonal and meridional winds with a 2 km height resolution in the
191 80-100 km height range. Because of the sometimes sparse number of meteor events per
192 hour (as low as 10) and the unpredictable nature of the natural geophysical variability at
193 time scales less than one hour, an estimate of the uncertainty in the velocity magnitude
194 itself has some error. For this system, in the early morning (21 UT) when the meteor
195 rates are high (several hundred per hour), the uncertainty is typically about 5 m/s, while
196 in the late afternoon (8 UT) when the rates are low (20 per hour), the uncertainty can
197 be as high as 20 m/s. At 14 UT an uncertainty of 10m/s would be representative.

198 **2.1.4. MF Radar at Buckland Park**

199 An MF radar is located at Buckland Park, some 35 km north of Adelaide, Australia.
200 Operating at 1.98 MHz it measures winds using the spaced antenna technique in the 60-98
201 km range by day and 80-98 km range by night. Measurements are made every 2 minutes at
202 2 km height intervals. Here we use hourly average zonal and meridional wind components.
203 Further details about the system and techniques used may be found in *Holdsworth and*
204 *Reid* [2004].

205 **2.1.5. SABER instrument on TIMED**

206 The Sounding of the Atmosphere using Broadband Emission Radiometry (SABER) ex-
207 periment is one of four instruments on the Thermosphere Ionosphere Mesosphere Energet-
208 ics and Dynamics (TIMED) satellite [Russell *et al.*, 1999]. SABER scans the atmospheric
209 limb vertically and observes emission in 10 broadband spectral channels. Version 1.07
210 kinetic temperatures are retrieved from CO₂ 15 μ m limb emission measurements at ap-
211 proximately 2 km vertical resolution (e.g. [Mertens *et al.*, 2001; Remsberg *et al.*, 2008]).
212 The limb tangent points (at 85 km) used below are shown in Figure 1.

213 **2.1.6. TIDI instrument on TIMED**

214 The TIMED Doppler Interferometer (TIDI) instrument on the TIMED satellite provides
215 profiles of winds in the upper mesosphere and lower thermosphere [Killeen *et al.*, 1999;
216 Skinner *et al.*, 2003; Niciejewski *et al.*, 2003]. The TIDI winds have undergone a recent
217 recalibration and in this paper version 10 data are used. We found that only one of the two
218 lines of sight on 31 January 2006 at approximately 1415 UT provided data over nighttime
219 Australia that could be used to track the relative variation of the wind speed from north
220 to south across the continent. This wind direction was approximately 116 degrees east of
221 north which fortuitously is the closest to the direction of the observed AGWs over Alice
222 Springs described later in this study. Those AGWs propagate at about 150 degrees east
223 of north. The data points are at 2.5 km intervals from 80 to 100 km altitude. At 85(97.5)
224 km altitude the 1 sigma uncertainty is about 30(10) m/s. The limb tangent points (at 85
225 km) used below are shown in Figure 1.

226 **2.1.7. ECMWF**

227 Winds and temperatures up to an altitude of about 50 km were obtained from the
228 output of the operational analysis from the European Center for Medium-Range Weather
229 Forecasts (ECMWF) assimilation data for 12 UT on 131 January 2006 (e.g. [*Hamilton et*
230 *al.*, 2004]). The ECMWF data are provided as 1.125 by 1.125 degree grid points. Here
231 the point centered at -19.5° south latitude and 130.5° east longitude was used as shown
232 in Figure 1.

233 **2.1.8. HWM/URAP**

234 A major unknown is connecting the ECMWF profile at 50 km with the measured
235 radar wind profiles in the upper mesosphere. Two estimates of winds in this region are
236 available, those from the Horizontal Wind Model (HWM) [*Hedin et al.*, 1996] and those
237 from the Upper Atmosphere Research Satellite (UARS) reference atmosphere project
238 (URAP) [*Swinbank and Ortland*, 2003]. Both are based on climatologies and the latter is
239 only available for zonal winds. The data used here on 31 January 2006 are from 12 UT,
240 at -20° south latitude, and 135° east longitude. This location is shown in Figure 1

2.2. Adopted Winds and Temperatures

241 In order to analyze the data using analysis techniques described below, temperature
242 and wind profiles were first constructed.

243 **2.2.1. Temperature Profile**

244 Figure 2 shows the temperature profile used for the ray trace analysis that is taken from
245 the SABER overpass on 31 January 2006 at 1413 UT. The adopted profile has a tangent
246 altitude at approximately 18.38° south latitude and 132.55° east longitude as shown in
247 Figure 1. This location is the closest SABER profile in distance (and in time) to the
248 tropical storm that is the presumed source of the observed AGWS and to the ECMWF

249 data used for the winds. For comparison the model temperature profile from ECMWF is
250 also shown. The ECMWF analysis was for 12 UT at approximately 19.5° south latitude
251 and 130.5° east longitude close to the center of the rainfall discussed below.

252 **2.2.2. Wind Profiles**

253 Here we discuss the derivation of the zonal (U) and meridional (V) wind profiles from
254 15 to 100 km. These profiles are based partly on data (below 50 and above 84 km) and
255 partly on climatology (between 50 and 84 km). In particular, the meridional and zonal
256 wind profiles up to about 50 km are the ECMWF profiles which, as noted above, are
257 obtained at 12 UT on 31 January 2006 at a location of 19.5° south latitude 130.5° east
258 longitude.

259 Above 84 km available data existed at Darwin and BP. Since the region of interest is
260 south of Darwin and near AS we produced a wind profile at and above 84 km based on
261 the following considerations. Figure 3 shows measured winds at Darwin and BP at 88
262 km altitude for the period from 29 January to 2 February 2006 from the meteor and MF
263 radars. Overall the winds are weaker at BP than at Darwin. Since AS is nearly halfway
264 between Darwin and BP we simply averaged these data sets (from 84 to 98 km) to produce
265 a wind profile to be used for this analysis at and above 84 km. At 100 km we used the
266 Darwin data.

267 There is a strong quasi two day wave (QTDW) at Darwin in the meridional component.
268 The wavelet analysis techniques outlined in *Torrance and Compo* [1998] allow an estimate
269 of the strength of the diurnal tide and the QTDW components. The meridional compo-
270 nents at 88 km have amplitudes of approximately 40 m/s for the QTDW and 44 m/s for
271 the tide. The zonal components are weaker being 12 m/s for the QTDW and 37 m/s

272 for the tide. The uncertainties are about 12 m/s. The QTDW also appears, but much
273 weaker, at BP where the zonal(meridional) component of the QTDW is about 12(16) m/s
274 with an uncertainty of 15 m/s. The tide appears strongly in the BP data, as it does at
275 Darwin, with both components having amplitudes of between 20 and 25 m/s.

276 As a further qualitative check on this approximation Figure 4 shows the TIDI wind
277 profiles for the one line of sight that was available across Australia at locations shown
278 in Figure 1 at about 1415 UT on 31 January 2006. Also shown are the BP and Darwin
279 profiles at 14 UT rotated to match the direction of the TIDI line of sight. The TIDI
280 winds and ground-wind data generally overlap considering the error bars but there are
281 some places where this does not occur, notably between the TIDI1 data and the Darwin
282 data near 93 and 95 km. Note however, that the TIDI1 tangent point (shown in Figure
283 1) is west of Darwin by about half an hour in local time. As shown in Figure 3 there
284 can be steep gradients in the wind components suggesting that a small phase difference
285 in time could be responsible for this mismatch. Furthermore, the TIDI winds are line of
286 sight winds that smooth out wind variations due to AGWs while the Darwin radar winds
287 see a different smoothing depending on the distribution of meteor echos. Also note that
288 the TIDI winds are over obtained over a much shorter period of time (seconds) than the
289 Darwin winds which are averaged over an hour.

290 Despite these differences in a detailed comparison, it is clear there are many similarities,
291 the most important of which is the change in the magnitude from north to south. Thus,
292 our approximation of averaging the Darwin and BP profiles to provide winds in the vicinity
293 of Alice Springs seems reasonable as a first approximation. However, the presence of the
294 strong QTDW, especially at Darwin, does complicate the choice of a characteristic wind

295 to be used above 84 km. In a later section where this analysis is further considered we
 296 will revisit this portion of the wind profile.

297 Above 50 km these need to join the adopted profiles above 84 km, that are based on
 298 measured winds at Darwin and BP, with winds in an altitude region where no measured
 299 data exist. We used HWM model data, which gives results for both zonal and meridional
 300 components, for that region. Based on these two profiles (ECMWF below 50 km and the
 301 adopted radar-based profile above 84 km) we constructed the wind profile from 50 to 84
 302 km based on HWM. We assume a linear interpolation of the winds for both the zonal and
 303 meridional components. Figures 5-6 show the final adopted profiles and the HWM model
 304 results.

305 We note however that the URAP model has a steeper decline in the zonal component
 306 from approximately 50 to 65 km than our adopted profile. Given the dynamic effects that
 307 can occur above 50 km the adopted profiles are plausible. However, we will also comment
 308 later on the differences that can occur in our analysis if we use the URAP type profile.

2.3. AGW Analysis Techniques

309 The analysis of AGW intrinsic parameters follows from the dispersion relations shown
 310 below (e.g. *Hecht* [2004a]). Consider an AGW at an altitude z above the ground in an
 311 atmosphere where H is the density scale height. The vertical wavenumber, m , is given by
 312 $2\pi/\lambda_z$, where λ_z is the vertical wavelength. The vertical wavenumber obeys the following
 313 dispersion relation

$$m^2 = (2\pi/\lambda_z)^2 = \frac{(N^2 - \omega_I^2)(k^2 + l^2)}{(\omega_I^2 - f^2)} + \frac{\omega_I^2}{c_s^2} - \frac{1}{4H^2} \quad (1a)$$

$$m^2 = \frac{(N^2 - \omega_I^2)(k^2 + l^2)}{(\omega_I^2 - f^2)} + \frac{(\omega_I^2 - \omega_a^2)}{c_s^2}. \quad (1b)$$

314 In equation (1a), c_s is the speed of sound, ω_I is the intrinsic frequency, that is the
 315 frequency measured in the frame of reference that moves with the background wind, and
 316 f is the inertial frequency which is $2\Omega\sin(\phi)$, where ϕ is latitude and Ω is the angular
 317 speed of the earth. Also k and l are the vector components of the horizontal wavenumber,
 318 k_h , whose magnitude, $(k^2 + l^2)^{0.5}$, is equal to $2\pi/\lambda_h$. For a given background wind velocity
 319 component, \bar{u} , in the direction of k_h , and an observed wave horizontal phase velocity, c_o ,
 320 the intrinsic wave phase velocity, c , is given by $c_o - \bar{u}$ which is equal to ω_I/k_h . The observed
 321 (ground-based) period, τ_g , is equal to λ_h divided by c_o . The intrinsic period, τ_I , is equal
 322 to λ_h divided by c . In equation (1b) the acoustic cutoff frequency, ω_a , is given by $c_s/(2H)$
 323 in an isothermal atmosphere. Note that when m^2 is negative the AGW is evanescent and
 324 it is not freely propagating vertically. Such a region can form a boundary for a trapped
 325 or ducted AGW.

326 We note that the use of the term freely propagating here, and throughout the paper,
 327 simply means that m^2 is positive. Such AGWs could still be subject to viscous dissipation
 328 and lose energy (e.g. [*Gossard and Hooke, 1975*]) especially as m becomes large but such
 329 damping is not considered here.

330 2.3.1. AGW Ray Tracing

331 Since this work is concerned with possible sources of the AGWs seen in airglow images,
 332 it is instructive to incorporate ray-tracing techniques into the analysis. Ray-tracing tech-
 333 niques are used to investigate the effects of background wind and temperature variations
 334 on gravity wave propagation. These techniques, as applied to AGW propagation, are well

335 summarized in *Jones* [1969], *Marks and Eckermann* [1995], *Eckermann and Marks* [1996],
 336 and *Lighthill* [1978].

337 For waves with a dispersion relationship $G(k, l, m, x, y, z)$ where (x, y, z) is the
 338 position vector, (k, l, m) is the wavenumber vector, and t is time, the following equations
 339 describe the ray path and the refraction of the wavevector along the ray where the time
 340 derivatives are following the group motion of the ray packet.

$$dx/dt = \partial G / \partial k \quad (2a)$$

$$dy/dt = \partial G / \partial l \quad (2b)$$

$$dz/dt = \partial G / \partial m \quad (2c)$$

$$dk/dt = -\partial G / \partial x \quad (3a)$$

$$dl/dt = -\partial G / \partial y \quad (3b)$$

$$dm/dt = -\partial G / \partial z \quad (3b)$$

341 Equations 2-3 show how the ground-based group velocities and the wavevectors are
 342 modified by spatially varying winds and temperatures.

343 Following *Marks and Eckermann* [1995], the non-hydrostatic dispersion relation appro-
 344 priate for gravity waves on a slowly varying background flow is expressed as

$$\omega_I^2 = (\omega_o - Uk - Vl)^2 \quad (4a)$$

$$\omega_I^2 = \frac{N^2(k^2 + l^2) + f^2(m^2 + 1/(4H^2))}{k^2 + l^2 + m^2 + 1/(4H^2)} \quad (4b)$$

345 where ω_o is the ground-based frequency. From Equation 4 an expression for m, the vertical
346 wavenumber, follows as

$$m^2 = \frac{(k^2 + l^2)(N^2 - \omega_I^2)}{\omega_I^2 - f^2} - 1/(4H^2) \quad (5)$$

347 Equations 4 and 5 differs from equations 1a-1b in that they neglect a term ω_I^2/c_s^2 but for
348 the wave frequencies considered here this term is negligible. Furthermore, terms including
349 f are also negligible for the wave frequencies considered in this work. Thus, for the AGWs
350 considered here the difference in m derived from equations 1a-1b and 5 can be ignored as
351 it is on the order of 1 percent or less. Equations 4 and 5 can then be used to derive, via
352 Equations 2-3, the group trajectory of the wave packet through the atmosphere.

353 For this work ray tracing was performed with the assumption that the atmospheric
354 wind and temperatures are considered spatially invariant in x and y and time invariant.
355 The resulting equations, which use $\Delta = k^2 + l^2 + m^2 + \alpha^2$, where $\alpha = 1/(4H^2)$, are found
356 in Appendix A of *Marks and Eckermann [1995]*. In Equation 6d the subscript z means
357 taking the spatial derivative of the given quantity with respect to z.

$$dx/dt = U + \frac{k(N^2 - \omega_I^2)}{\omega_I \Delta} \quad (6a)$$

$$dy/dt = V + \frac{l(N^2 - \omega_I^2)}{\omega_I \Delta} \quad (6b)$$

$$dz/dt = \frac{-m(\omega_I^2 - f^2)}{\omega_I \Delta} \quad (6c)$$

$$dm/dt = -kU_z - lV_z - \frac{(N_z^2(k^2 + l^2) - \alpha_z^2(\omega_I^2 - f^2))}{2\omega_I \Delta} \quad (6d)$$

358 There are several ways to perform a raytrace. We chose to solve these coupled equations
 359 using a fourth order Runge-Kutta algorithm (RK4), as supplied in the Interactive Data
 360 Language (IDL) which is based on the algorithms in *Press et al.* [1993]. The wave packet
 361 was launched at 15 km altitude (z_0) and at a starting position (x_0, y_0), the location of
 362 the storm that generated the AGW. Equation 5 was used to calculate the initial value of
 363 m . The group trajectory and wavenumber were then obtained by numerically integrating,
 364 using RK4, Equations 2 and 3 with respect to time along the group trajectory, using a
 365 time step of 10 s. This procedure allowed the calculation of the distances ($\delta x, \delta y, \delta z$)
 366 travelled in all three spatial dimensions during this 10 second time step. The ray was
 367 then relaunched from the new starting position, after recalculating m using Equation 5,
 368 for another 10 seconds and this was continued until the packet reached a given altitude,
 369 40 km for the AIRS data and 85 km for the airglow data, or until m^2 is negative indicating
 370 that the AGW is evanescent.

371 As a practical alternative we also calculate horizontal and vertical group velocities,
 372 using equation 5 to calculate m at the beginning of each interval, and Equations 6a, 6b,
 373 and 6c to calculate ($\delta x, \delta y, \delta z$), varying the time steps so that δz is 1 km. This is done
 374 for every altitude in 1 km intervals from 15 km where a wave packet is launched. This

375 is repeated until either the packet reaches a given altitude noted above, or until m^2 is
376 negative indicating that the AGW is evanescent. In this approach it is assumed than m
377 is constant over each altitude step but as this is an approximation an error is induced.
378 However, this error is small as long as the variation of m is small.

379 For the analysis in this work the difference between the two approaches is small (a few
380 percent). Most of the results were calculated using the RK4 method. The alternative
381 method was used, however, for for the calculations of trapped AGWs above 85 km which
382 are discussed next.

383 **2.3.2. Trapped AGWs**

384 Some of the AGWs considered here reach 85 km altitude rapidly, in under an hour,
385 travelling only a short distance horizontally from the storm center still many hundreds
386 of kilometers from Alice Springs. However, in certain launch directions an AGW can
387 encounter an evanescent region between 65 to 80 km a few km thick. If there also exists
388 an evanescent region just above the airglow layer (say 100 km) then a trapped region
389 exists. In an ideal case where the vertical wavelength of the wave is some multiple of the
390 vertical distance of the trapped region a duct can exist.

391 The problem of how to treat the propagation of trapped or ducted AGWs in the
392 mesopause region. Here we equate trapping with the generic reflection of waves between
393 an upper and lower boundary while a duct includes only those few trapped modes that
394 are resonant. This has generated considerable interest in recent years since *Walterscheid*
395 *et al.* [1999] suggested that many of the waves seen in ground-based airglow imagers may
396 be ducted, perhaps a thermal duct that often occurs because of the nominal temperature

397 structure of the 80 to 140 km region. *Snively and Pasko* [2008] is a recent work that
398 discusses the ducting problem in this altitude region and many useful references are cited.

399 There are at least two potential problems with hypothesizing ducted AGWs in the
400 mesopause region. First, because of the large variability, spatially and temporally, of
401 mesopause winds and temperatures, due to the presence of large amplitude waves and
402 tides, the duct properties could change considerably. Thus, it is difficult to see how a
403 perfectly ducted wave would exist for a long (multi-hour) period. Second, how does a
404 wave enter the duct. If it is easy to enter when the duct is leaky, while a rigid duct would
405 cause too much wave energy to be lost on entry.

406 *Hecht et al.* [2001] tried to address these concerns by assuming that instead of a duct
407 the AGW was trapped by regions below and above the airglow layer. In this model a
408 wave passes through the lower evanescent region losing some energy. The wave packet
409 then freely propagates vertically and horizontally until it reaches the upper evanescent
410 region. The wave is then reflected down, losing some energy, and propagates until it
411 reaches the lower region where it is reflected again losing some energy. For different
412 thicknesses of evanescent regions, that were typical of what AGWs seen in airglow imagers
413 might encounter, *Hecht et al.* [2001] calculated how far such an AGW would propagate
414 horizontally until its amplitude was about 10 percent of the original amplitude. In such a
415 case and assuming the original amplitude would produce a few percent density (or airglow
416 temperature) perturbation, the resultant trapped wave would then produce a temperature
417 perturbation of a few tenths of a percent. However, because the perturbation of the airglow
418 intensity amplitude is five to ten times the airglow temperature amplitude, such AGWs
419 would still be visible in airglow images. It was estimated that such AGWs might be able

420 to propagate 1000 km or so. While this model was quite simple it did show that even if
421 the trapped region did not allow for the formation of a perfectly ducted standing wave, it
422 was possible for AGWs to propagate horizontally a considerable distance away from the
423 source. The trapped region would also select out certain vertical wavelength waves since
424 those would preferentially have the highest amplitudes after travelling a given horizontal
425 distance. Furthermore, as long as there existed a trapped region below there probably
426 always existed a trapped region above 100 km (nominally around 105 km) due to the large
427 winds that seem to exist almost continuously at the base of the thermosphere [*Larsen,*
428 2002].

429 We use here the same simplified approach that was performed in *Hecht et al.*
430 [2001, 2004b]. Once the wave packet reached 85 km the wave was assumed to be trapped
431 between layers of evanescence. In the trapped region the wave packets are assumed to
432 be freely propagating, bouncing back and forth between layers of evanescence. We use
433 the alternate ray trace approach to calculate the time it takes for the AGW to propagate
434 vertically between two fixed altitudes that are between the bottom and top evanescent
435 regions. (However, as we note later, because of uncertainties in the available winds we
436 restrict the region of vertical propagation to that where measured winds are available.)
437 We also calculate the horizontal distance, with respect to the ground, that is travelled
438 during this period. This is then used to calculate how far (and how many bounces occur)
439 over some multiple of this period. Thus, we can estimate, given an initial propagation
440 direction, the location of the AGW after a given amount of time. We note though that
441 although this simplified approach ignores the effects of winds at the boundaries where the

442 waves are evanescent, these effects should be small since the packet spends most of the
443 time in the free propagation region.

444 This however, also ignores the time it takes for the AGW to traverse the evanescent
445 region to reach 85 km. This time can be estimated as follows. While the group velocity in
446 the evanescent region is undefined following *Walterscheid and Hecht* [2003] one can define
447 a energy flow velocity in the vertical as $U_f = F/E$, where F is the wave energy flux and E
448 is the wave energy density. U_f is equal to the vertical group velocity, w_g , just below the
449 base of the evanescent region. To estimate U_f for the evanescent layer we set $F = TF_o$,
450 where F_o is the incident flux and T is the transmission coefficient for the layer; for an
451 infinite evanescent layer $T=0$, but otherwise it is nonzero. Thus $U = Tc_g$ where T can be
452 calculated following *Hecht et al.* [2001]. *Walterscheid and Hecht* [2003] also gives formulas
453 for the horizontal group velocity in the evanescent region. While these strictly only apply
454 to isothermal atmospheres we apply these to our nonisothermal atmosphere to estimate
455 horizontal propagation since for the parameters considered N is still much greater than
456 ω_a .

3. Results

3.1. Overview

457 In this study we concentrate on a period during which a strong isolated tropospheric
458 rainfall source was present and determine whether AGWs could be identified in both the
459 ground-based imager data and in the AIRS data. The period we chose to investigate was
460 from 28 January to 31 January 2006 with a location over northern Australia. The reason
461 for choosing these dates is that the Tropical Warm Pool International Cloud Experiment
462 (TWPICE) [*May et al.*, 2008] occurred during this period. This experiment was designed

463 to study, in detail, the evolution of tropical cloud systems over northern Australia during
464 a period when large monsoon events are known to occur. In late January 2006 a large
465 tropical low came onshore. In their TWPICE overview paper *May et al.* [2008] describe
466 this as an event that would have become a tropical cyclone over water had it remained
467 offshore. Instead it established itself as an almost stationary low with a well defined trop-
468 ical cyclone like cloud field over land between AS (Alice Springs) and Darwin for several
469 days (26 January to 1 February 2006) causing extensive flooding. This low continued to
470 intensify as it moved inland and formed a well defined tropical cyclone like cloud field.
471 The lowest surface pressure recorded from this event was 988 hPa on 31 January 2006.
472 During its intensification it contained a number of well defined convective bursts as seen
473 from significant areas of cloud. These clouds had brightness temperatures, obtained from
474 the Japanese geostationary satellite MTSAT-IR (e.g. [*May et al.*, 2008]), that were sim-
475 ilar to or colder than the tropopause temperature. This low was also associated with
476 considerable convective and stratiform rainfall. While soundings are not available in the
477 area of the storm, the CAPE that was recorded as the low passed through Darwin on
478 24-25 January 2006 was above 2000 J/kg [*May et al.*, 2008], indicating the potential for
479 significant strong updrafts. The cloud field associated with the low exhibited many of
480 the characteristics of a developing tropical cyclone, and these often contain significant
481 updrafts even in the absence of high values of CAPE.

482 Another technique to establish the potential for convective activity is to look at cloud top
483 temperatures also obtained from MTSAT-IR (e.g. [*May et al.*, 2008]). Figure 7 highlights
484 the larger and relatively constant coverage of clouds with brightness temperatures (T_B)
485 warmer than about 220 K, and the increases in deep convective activity with T_B colder

486 than the tropopause cold point (approximately 190 K), indicating overshooting cloud tops.
487 This deep convection maximized between about 12 UT (2130 local time) and 15 UT each
488 day during the intensification of the storm system. There was a rapid decay in the deep
489 convection after about 12 UT on 31 January 2006 although heavy rain persisted for about
490 another day.

491 Figure 8 shows a 24 hour rainfall map issued for six periods. Two of the periods, the first
492 and last, are for comparison with the tropical low plots. The first is on 19 January 2006
493 which shows strong monsoon rainfall typical of the early part of the TWPICE experiment
494 with widespread oceanic convection. Oceanic convection is typically characterised by
495 modest updraft strength (e.g. [*Keenan and Carbone, 1992*]). The period on 4 February
496 2006 shows minimal convective activity.

497 The other four plots show the period of the tropical low from 28 January 2006 to 31
498 January 2006 UT. Note that because of the lack of data the rainfall in central Western
499 Australia, typically in the region between 120° and 130° east longitude and 20° to 30°
500 south latitude, is often not reported. There are three significant regions of rainfall during
501 this period. The most intense is that associated with the tropical low that was northwest
502 of AS. While there is significant rainfall due to the low on 28 January 2006 the rainfall
503 intensified over a small region over the next few days. The most intense rainfall sampled
504 by the rain gauge network occurred on 31 January 2006 when almost 250 mm of rain fell
505 northwest of AS, although it is likely a significant fraction of the rain was stratiform in
506 origin (e.g. [*Houze, 1993*]). By this time the cloud structure of the storm system was
507 similar to a tropical cyclone. Note that the upper level outflow region of such storms are
508 close to inertially neutral and may also be a source of gravity waves [*May et al., 1994*] in

509 addition to the direct convective sources indicated by the very cold cloud tops. Thus, this
510 is an ideal isolated rainfall event to study with respect to AGW generation.

511 Note that the maps show that even though most of the rainfall was northwest of AS there
512 were still patches of rain east of the low. A second region of rainfall was on the Cape York
513 Peninsula in the extreme northeast portion of Australia. As this is the wet season monsoon
514 rain falls nearly continuously at some locations across northern Australia. However, a
515 statistical study of AGWs has shown, that at least with respect to airglow images, few
516 AGWs seem to originate from the east and propagate to the west [*Walterscheid et al.*,
517 1999]. The third region of rainfall appears associated with a band of rainfall that is
518 moving from the western coast eastward across mainly the central and southern part of
519 the continent. This occurred from 29 to 31 January 2006. On January 28 there is also
520 considerable rainfall along the northwestern coast. Since the most intense isolated rainfall
521 occurred on January 31, and there were also good data available from the ground station
522 at AS, most of the analysis will concentrate on that day. However, some comments will
523 also be made about data from the other days.

3.2. AIRS Results

524 The AIRS data are L1b radiances in $\text{mW}/\text{m}^2\text{-sr-cm}^{-1}$ that can be converted into bright-
525 ness temperatures (e. g. [*Alexander and Barnett, 2007; Alexander and Teitelbaum, 2007*]).
526 To identify AGWs these radiance maps must be analyzed to look for deviations from the
527 mean. The channel we have chosen is in the narrow CO_2 band centered at 667.8 cm^{-1}
528 that has a broad vertical weighting function of nearly 12 km width, and that peaks near
529 40 km altitude.

530 Figure 9 shows maps of these radiance perturbations, from three dates (19 January,
531 31 January, and 4 February 2006) of Figure 8, with an overlay of the largest rainfall
532 contours. Note that the colorbar levels only apply within the image swath. The one
533 sigma noise level is $0.24 \text{ mW/m}^2\text{-sr-cm}^{-1}$. The top image from 19 January 2006 shows
534 intense curved perturbations that may be associated with an AGW radiated from the
535 monsoon rainfall over northern central Australia. The middle image from January 31
536 clearly shows strong perturbations, exceeding the three-sigma noise level, centered to the
537 northwest of Alice Springs near the largest rainfall contours of the tropical low. The region
538 of largest negative perturbation appears just to the west of the rainfall event contours.
539 Most of the perturbations appear to be symmetric around this region. The bottom image
540 from 4 February 2006 shows little evidence of intense perturbations consistent with low
541 rainfall on this date. Most of the rest of the analysis will concentrate on the 31 January
542 2006 image event.

543 The results of the wavelet analysis for 31 January 2006 are shown in the next two
544 figures. Figure 10 shows the directionality of k_h (with a 180 degree uncertainty) for these
545 waves. We only used regions where the amplitudes of the retrieved waves are above 0.48
546 $\text{mW/m}^2\text{-sr-cm}^{-1}$, which is a signal to noise (S/N) of 2. We also assume that eastward
547 propagation with respect to the ground is favored east of a region of strong convection.
548 The large white arrows show movement to the E, NE and SE consistent with AGWs
549 originating near the storm center. Interestingly, over AS, where our airglow imager was
550 observing AGWs above 80 km, the AGW phase propagation at 40 km is towards the SE.
551 We note there are other arrows (directions) that are not associated with the large storm.
552 They could be due to other smaller rainfall systems. We have also not plotted results

553 from near the edges of the AIRS image swath as they can suffer greater uncertainty in
554 the analysis due to wavelet wrap-around edge effects [*Alexander and Barnet, 2007*].

555 The wavelet analysis also captures the amplitude of the dominant waves. Figure 11
556 shows their amplitudes with the rainfall contours superimposed. A cutoff of $0.72 \text{ mW/m}^2\text{-}$
557 sr-cm^{-1} , an S/N of 3, has been used in this plot. Note that this does not show phase
558 fronts but simply, at any location, the amplitude of the dominant AGW. The maximum
559 amplitude is around $1.5 \text{ mW/m}^2\text{-sr-cm}^{-1}$, that is approximately an S/N of over 6. The
560 associated brightness temperature amplitude is 1.6K and the true temperature amplitudes
561 will be larger than this by an unknown factor that depends on the vertical wavelength of
562 the wave. Vertical wavelength cannot be directly determined from these data. The largest
563 perturbations occur in the region of the rainfall event, although slightly to the west.

564 To understand the origin of these waves a ray trace was performed with a horizontal
565 wavelength of 300 km, since the wavelet analysis revealed wavelengths between 200 and
566 400 km. Two observed periods were used, 120 or 25 minutes. The 120 minute value, which
567 was chosen to approximate the maximum AS observed periods discussed below, results in
568 vertical wavelengths, at 40 km altitude, varying for example from about 33 km for AGWs
569 launched due east (90 degrees east of north) to about 20 km when they are launched
570 towards AS. These values are all well above the approximate 12 km vertical weighting
571 function of this particular AIRS channel [*Alexander and Barnet, 2007; Alexander and*
572 *Teitelbaum, 2007*]. The 25 minute period waves freely propagate nearly as vertical as
573 is possible, for a 300 km λ_h AGW, up to 40 km altitude. AGWs with shorter periods
574 encounter an evanescent region below 40 km.

575 Figure 12 shows white lines which represent the results of the raytrace to 40 km altitude
576 for AGWs, with varying horizontal propagation azimuths, generated at 15 km altitude at
577 the center of the largest rainfall contour. The two arcs are for the two different observed
578 periods that were used. For this example AGWs would be predicted to be present at
579 40 km only at the positions of these two arcs. AGWs with periods between 25 and 120
580 minutes would occur between the two arcs. Note that the results of Figure 12 show only
581 that an AGW reaches that distance from the center of the rainfall at some time. Thus, the
582 300 km 120 minute AGWs that are launched due east reach 40 km altitude in about 100
583 minutes. However, the wave launched at 30 degrees east of north reaches 40 km altitude
584 in 140 minutes. So the phase of the wave at 30 degrees may be quite different. Thus, the
585 line giving the locations where specified waves intersect 40 km is not a line of constant
586 phase. This is true to a lesser extent for the shorter 25 period AGWs (which have fast
587 phase speeds) as these waves even when launched from different azimuths mostly arrive
588 at 40 km at similar times.

589 The AIRS images show some morphological differences in their phase front orientations
590 from this simple analysis. Because of the extended nature of the source in space and
591 in time, and the generation of a spectrum of AGWs, interference effects between AGWs
592 probably account for these differences. Also of interest is what generates the AGWs seen
593 to the east of the circles in Figure 12. This will be discussed further below.

3.3. Alice Springs (AS) Results

594 3.3.1. Long-Period Large-Horizontal Wavelength AGWs

595 The ray trace analysis, using the adopted wind and temperature profiles, indicates that
596 several hundred km λ_h waves with observed periods of a few tens of minutes or more

597 should reach 85 km without encountering an evanescent region. Thus, such waves should
598 be visible in the AS airglow data. While such waves cannot be directly seen in the images
599 because they are larger than the field of view, techniques have been developed that allows
600 the detection of such AGWs and their approximate horizontal wavelengths, e.g. *Hecht et*
601 *al.* [1997].

602 The top panel in Figure 13 shows the OHM brightness measured by the AS imager on
603 31 January 2006 UT. The solid line is the image average over an approximately 58 x 90 km
604 box while the dotted line is an average over an approximate 10 x 16 km box. There were a
605 few images, indicated by diamonds, where clouds obscured some stars. Since the presence
606 of clouds can affect the ability to determine OHM brightness these data are not used in
607 the following discussion. However, it should be noted that because clouds scatter light
608 back into the field of view [*Gattinger et al.*, 1991] the brightness data may not necessarily
609 be affected. Over most of the cloud-free period what is seen are wavelike oscillations with
610 ground-based periods on the order of 1 to 2 hours. The perturbation in intensity is on
611 the order of 10 percent. However, because the imager also obtains temperatures we find
612 temperature perturbations (not shown) which are between 1 and 2 percent of the mean.
613 For the AGW around 1500-1630 UT the intensity and temperature perturbations, with
614 respect to the mean, are approximately 8 and 1.6 percent respectively. The ratio of these
615 two, the Krassovsky ratio, is 5 which is in the range of the predictions of *Schubert et al.*
616 [1991] for these AGWs.

617 There is a difference in amplitude between the two plots in the top panel. The bottom
618 panel shows that this difference is on the order of 2 to 3 percent. A model was constructed
619 where AGWs with different different λ_h values were propagated through the two average

620 boxes to determine how much the AGW amplitude was reduced. It was found that AGWs
621 with a λ_h of about 400 km or greater show a 2 to 3 percent difference in the peak amplitude.
622 Thus the λ_h from this analysis is close to the AIRS result suggesting that indeed similar
623 long wavelength waves are seen at both 40 and 85 km altitudes.

624 It is also possible to determine the propagation direction of the AGW by placing 9
625 boxes around the image, plotting the OHM intensity in each box, and looking for time
626 differences. This approach was used for example in *Hecht et al.* [1997]. Because there are
627 short-scale AGWs in the images (see below) this approach is found here to be somewhat
628 uncertain. It is clear that the 400 km λ_h AGW at around 15 to 16 UT is propagating
629 N to S and W to E. However, the exact direction (i.e, how many degrees east of north)
630 cannot be established. Nevertheless such a direction would be consistent with an origin
631 from the storm.

632 Ray traces were then performed, over varying horizontal propagation azimuths, for
633 AGWS with a λ_h of 400 km and a 120 minute ground-based period. These were all
634 launched at 15 km altitude and followed until they reached 85 km altitude, the base
635 of the airglow region. Figure 14 shows the results which indicate that such waves would
636 appear over the AS observing site in about 4 hours. Waves generated at 12 UT or before
637 would reach 80 km altitude over AS at or before 16 UT. Since the very coldest clouds
638 presumably associated with vigorous convective rainfall were present before about 12 UT
639 on January 31 the AGWs seen at AS were probably due to convection. Furthermore,
640 based on the top panel of Figure 13 the long period waves over AS were present prior
641 to 16 UT but appear to be of much lower amplitude after 16 UT. Thus, the long period
642 AGWs over AS may indeed be due to the convective activity that, based on Figure 7,

643 would be associated with the very cold clouds which occurred during the first half of 31
644 January 2006.

645 However, since the waves observed by AIRS took about 1.5 to 2 hours to reach 40 km
646 altitude (Figure 12) those were generated after 12 UT. Thus, it is not clear if the AIRS
647 perturbations are due to convectively generated AGWS or, as referenced earlier, AGWs
648 generated in the outflows of this tropical cyclone-like system.

649 **3.3.2. Short-Period Small-Horizontal Wavelength AGWs**

650 In addition to the long-period waves the images resolved short-period short-horizontal
651 wavelength AGWs that are similar to those typically seen in imagers in Australia and
652 elsewhere (e.g. [*Walterscheid et al.*, 1999; *Hecht*, 2004a]). Because of the smoothing used
653 to obtain Figure 13 these short-period waves are not resolved in these plots. However,
654 analysis of the individual images (not shown) reveals that those observed have λ_h values
655 from 30 to 45 km and ground-based periods of 15 to 25 minutes. While AGWs were
656 imaged throughout the night observation period from 11 to 19 UT, they were seen in
657 bursts, with most of the wave images being from 1100 to 1200 UT, and from 1300 to
658 1430 UT. However, there is some uncertainty on these times as some of the periods, such
659 as between 1210 and 1225 UT where waves were not seen, were contaminated by clouds.
660 The propagation directions, which mostly range from 135 to 160 degrees east of north,
661 are shown in Figure 11. The direction of phase propagation suggests that these AGWs
662 originate from the storm region.

663 To understand their origin a ray trace was again performed. Figure 15 shows the
664 potential problems in this approach. This shows two plots of the square of the vertical
665 wavenumber, m^2 , with and without winds, calculated for an AGW with a λ_h of 35 km

666 and a ground-based period of 15 minutes. Between 80 and 100 km there is a region that
667 would be a duct or trapped region if there was an evanescent region below. However,
668 without winds m^2 is positive up to and above 95 km, and there is no trapped region.
669 The solid line plots m^2 with winds for an AGW propagating 150 degrees east of north. A
670 trapped region is formed with regions of evanescence between 60 and 80 km and around
671 98 km. (The lack of good winds above 98 km makes it difficult to determine how far up
672 the evanescent region extends.) This trapped region (between 60- 80 and 98 km) exists
673 for AGWs with λ_h of 30 km and periods up to 25 minutes. As the λ_h increases to 45 km
674 the upper limit for the period is about 15 minutes.

675 Consider the propagation of the AGW up to 85 km. This cannot be rigorously calculated
676 in our approach for all propagation angles since the AGW has to tunnel through an
677 evanescent region. However, for AGWS with a 35 km λ_h and a 15 minute ground-based
678 period, and propagating less than 38 and greater than 173 degrees east of north, m^2 is
679 always positive and thus the trapped region vanishes given our assumed wind/temperature
680 profile. If the λ_h is increased to 45 km the propagation angles for freely-propagating AGWs
681 changes only slightly to less than 31 and more than 158 degrees east of north. AGWs
682 initially propagating between these angles will see the evanescent region. Note that it
683 is mainly the strong zonal winds that are westward below 80 km altitude in conjunction
684 with the temperature gradients that cause the trapped region to form. Thus, AGWS
685 propagating southward and westward freely propagate.

686 For the waves that encounter an evanescent region we follow the procedure outlined
687 earlier. This essentially assumes that the AGWs which encounter the evanescent region
688 (propagation directions smaller than 174 degrees for 35 km λ_h with 15 minute ground-

689 based period AGWs) can tunnel through it in a short amount of time. To calculate
690 the time it takes to travel to AS we assume that the once the AGWs tunnel through
691 the evanescent region they are trapped and then can freely propagate bouncing between
692 the upper and lower evanescent layers. As outlined earlier we can then calculate how far
693 horizontally the wave packet travels in a given amount of time. Thus, we can calculate,
694 for any given initial propagation direction where an AGW will be with respect to the
695 ground after a given amount of time.

696 Before discussing the results of these calculations we first comment on the vertical and
697 horizontal propagation in the evanescent layer. The vertical group velocity was calculated
698 from 15 to 96 km. If any evanescent region existed the time it took to traverse this region
699 was calculated. Based on Figure 15 these regions were of small vertical extent (less than
700 1 km), mainly in the region between 60 and 80 km, and it was found that since T was
701 above 0.95 the amount of time it took to traverse these regions was small, less than 1
702 minute. (We note even if the evanescent layers had a larger vertical extent, say 5 km,
703 with the same vertical wavenumber, the amount of time it would take to traverse the
704 region would be less than 5 minutes.) These times are small compared to the transit time
705 it took to reach 85 km if we only calculate the times for the vertical regions where the
706 waves are freely propagating. The calculated horizontal group velocities, with respect to
707 the background wind, in the evanescent regions were low (below 20 m/s) and thus, the
708 resultant group velocities with respect to the ground were mainly to the west. However,
709 even if we consider that it took five minutes to traverse vertically across the evanescent
710 layer the horizontal propagation distances were small (less than 30 km) and thus were
711 ignored.

712 Accepting the above assumption the amount of time and horizontal distance travelled
713 was calculated for the AGW during the vertical travel from 15 to 85 km. At that point
714 the AGW was assumed to be trapped between 80 and 96 km. These limits were arbitrary
715 based on the available radar wind data. In fact the lower trapped region is probably below
716 80 km while the upper trapped region could even be above 100 km and be due to the
717 presence of the large winds reported on by *Larsen* [2002]. Then the amount of time and
718 horizontal distance travelled was calculated as the AGW went from 80 to 96 km. The
719 AGW was then assumed to be reflected and this distance was taken as that for a single
720 reflection. The total distance travelled horizontally was the sum of the distance travelled
721 to reach 85 km plus the distance travelled after a given number of reflections.

722 Clearly, this is a simple approximation that also depends critically on the assumed wind
723 profile. We found that when we used the adopted wind profile, that is based on the average
724 of the radar winds from BP and Darwin at 14 UT, the AGW launched at an azimuth 150
725 degrees east of north for a λ_h of 45 km and a ground-based period of 15 minutes essentially
726 travelled southward. In 40 minutes the AGWs would reach 85 km but would be displaced
727 to the west 26 km by the time it reached 85 km altitude. The center of the rainfall is
728 about 600 km from AS and even the edges of the main rainfall contours are about 350 km
729 northwest (about 250 km west and north) of AS. Thus, freely propagating AGWs would
730 not reach AS. However, even trapped waves would not reach AS as the winds would cause
731 the wave packet to move slightly towards the west not towards AS located to the east.

732 However, based on the variations illustrated in Figure 3 the wind direction is changing
733 significantly during the preceding hours. At 88 km the meridional component is changing
734 from strongly northward at 7 UT to strongly southward at 19 UT. Thus we used several

735 different wind profiles to simulate the AGW launched at 150 degrees east of north. First,
736 we simply used the average of the wind profiles at 12 UT instead of 14 UT. For this
737 assumption after 4.3 hours (15 reflections) the AGU would be 155 km east and 270 km
738 south of where it was launched, still not reaching AS. To simulate as the TIDI data
739 suggest, that the wind amplitudes south of Darwin decrease at a more rapid rate with
740 respect to latitude, we produced a profile that was weighted three to one in favor of the
741 BP winds. In that case, after 3.1 hours the AGWs would travel about 300 km east and
742 260 km south. This AGW could have been launched at the edge of the storm (as indicated
743 by the rainfall contours shown in Figure 11) and be seen in the AS imager. If we used
744 wind profiles earlier than 10 UT the AGWs would not travel far enough south to reach
745 AS.

746 These results are very dependent on the wind profile which is not precisely known.
747 Thus, a more detailed analysis is not warranted. They do however, suggest that there
748 was a time period (10 to 14 UT) where favorable wind conditions existed for AGWs to be
749 seen over AS if they were launched from the direction of the storm. The sporadic nature
750 of the observations is probably in part due to the temporal variations in the wind profile.

4. Discussion

751 Many of the results strongly suggest that the observed AGWs are due to the large storm.
752 In particular three results stand out; (1) the curved wavefronts, shown in the wavelet
753 analysis of the AIRS data, (2) the largest amplitudes in the AIRS radiance perturbations
754 occur in the region around the largest rainfall produced by the tropical low, and (3) the
755 propagation directions of the AGWs seen in the AS imager. However, there are a number
756 of issues and questions that are raised by the data analysis.

4.1. Origin of Long Wavelength AGWs in the AIRS image outside of the ray trace area

757 There are two regions of interest, not discussed above, where apparent AGW phasefronts
758 are observed as can be seen in Figure 12. One is the region to the east of the 300 km λ_h
759 120 minute raytrace circle, and a second is the region interior to the 300 km λ_h 25 minute
760 period raytrace circle. The following two sections give some consideration as to the origin
761 of such waves.

4.1.1. AGWs east of the 300 km λ_h 120 minute period raytrace in Figure 12

763 There are several possibilities for how AGWs could travel from the storm and still be
764 observed by AIRS. (1) The raytrace calculations described above were done for AGWs
765 generated over the center of the storm. Some of the AGWs seen to the east could be
766 generated at the eastern edge of the rainfall contours. But this would not explain all
767 the AGWs that are seen especially those towards the eastern edge of the AIRS swath.
768 However, as noted earlier there was rainfall to the east of the contour region as can be
769 seen in Figure 8. Although the time of the rainfall is not available it is possible that
770 the perturbations seen to the east are related to those events. (2) There could be wave
771 dispersion as described by the following simplified analysis that illuminates aspects of what
772 the raytrace calculates with the complete dispersion relation. Note that the equations
773 presented on p 305 in *Lighthill* [1978] also show these aspects.

774 For AGWs the angle of the intrinsic group velocity to the vertical, in the frame of
775 reference of the wind (assumed to be in the k direction for this example), is easy to calculate
776 from Equation 5 in the approximation where $f \ll \omega_I \ll N$ and $m^2 \gg 1/(4H^2)$. Both
777 of these are approximately valid for the λ_h and period of the AGWs considered in this

778 section. The resultant equation, also discussed in *Lighthill* [1978] and *Alexander and*
 779 *Holton* [2004] is

$$\theta = \cos^{-1}((\omega_I)/N) = \cos^{-1}(k/m) \quad (7a)$$

$$\theta = \cos^{-1}((\omega_o - kU)/N) \quad (7b)$$

780 where ω_o is the observed frequency. Thus, for a given horizontal wavelength, as the vertical
 781 wavelength becomes smaller (or the intrinsic period becomes larger) the AGW propagates
 782 more horizontally, and thus reaches a given altitude further from the source. Consider
 783 two limiting cases of equation 7b, the first without winds being

$$\theta = \cos^{-1}(\omega_o/N). \quad (8)$$

784 Suppose the data show the longest observed period is 120 minutes. As the wave period
 785 changes the AGWs are dispersed with respect to θ , but the longest wave period (in this
 786 case 120 minutes) sets the limit on how far east the AGW can travel with respect to the
 787 ground (e.g.[*Alexander and Holton, 2004*]).

788 Now consider the other limiting case of equation 7b where the wind velocity is large
 789 (and in the opposite direction to) the observed AGW phase velocity. The angle is now
 790 given by

$$\theta = \cos^{-1}(kU/N). \quad (9)$$

791 The intrinsic frequency becomes large (but still smaller than N) so that vertical wavelength
 792 is large. But in this case the angle now depends on the AGW horizontal wavelength. So
 793 now the AGWs are dispersed in θ based on the horizontal wavelength. So for a given

794 period, say 120 minutes, an 800 km λ_h AGW will travel further east than a 700 km λ_h
795 AGW. (But because the wave packet is advected westward by the winds they do not travel
796 as far east as the windless cases. This can be seen explicitly in the equations derived by
797 *Lighthill* [1978] on page 334 and in the complete ray trace analysis using Equations 6a-d
798 performed for this work.) The transition between these two regimes occurs when the
799 AGW phase velocity has the same magnitude as the wind velocity in the direction of the
800 AGW. For our wind profile at 40 km altitude this occurs for a 300 km λ_h , 90 minute
801 ground-based period AGW.

802 As the above analysis suggests when we raytrace AGWs with a 120 minute ground-
803 based period and λ_h values above 300 km (all with vertical wavelengths larger than 30
804 km) we find these AGWs can travel significantly further east. For example an 800 km λ_h
805 AGW travels nearly twice as far as the 300 km λ_h AGW. Furthermore, if we raytrace a
806 700 km λ_h AGW, it appears about 40 km closer when it reaches 40 km altitude compared
807 to the 800 km λ_h AGW. Thus, it is likely that the interpretation of the separation of
808 the phasefronts at distances far removed from the source may not be as simple as the
809 horizontal wavelength. It is possibly due to the different arrival times of long horizontal
810 wavelength AGWs of slightly varying periods and wavelength. Alternatively, as noted
811 above rainfall, albeit at lower levels, also exists east of the main low (see Figure 8) and
812 AGWs generated from convective sources associated with this rainfall will also contribute
813 to the observations.

814 **4.1.2. AGWs directly over the tropical low and interior to the 300 km λ_h 25**
815 **minute period raytrace in Figure 12**

816 The AGW raytrace shows that there is a zone above the tropospheric source into which
817 AGWs, especially if their λ_h values are near 300 km, will not propagate if they originate
818 from the center of the rainfall contours. This is represented by the interior of the inner
819 circle of Figure 12. For AGWs to reach this region they either are generated at the out-
820 ermost rainfall contours, or the waves are not internal AGWs but are internal acoustic
821 waves. Acoustic waves have been shown to be able to travel along vertical rays *Walter-*
822 *scheid et al.* [2001] but they have not been observed to date in any of our image data and
823 especially at stratospheric altitudes are apt to have very small amplitudes.

4.2. Persistence of the Trapped Region

824 The ability of short-wavelength short-period AGWs to reach AS requires a duct or
825 trapped region that exists for several hours. The temperature profile measured by SABER,
826 which shows an inversion between 80 and 100 km, predisposes the atmosphere to form
827 a trapped or ducted region. The actual formation of this region however, depends on
828 a suitable wind profile. We note that if we used the URAP instead of the HWM wind
829 profile, trapping would be suppressed. Thus, as the winds change the trapped region
830 turns on and off, suggesting that the trapped AGWs may not be continuously present
831 but could appear in bursts as was indeed observed. An alternative explanation, however,
832 could be that the source is intermittent. However, the source during TWPICE was quite
833 persistent over several days.

834 Because winds are quite variable it has been difficult in previous studies cited earlier
835 to understand how ducts or trapped regions can persist for the many hours required for
836 propagation of short horizontal wavelength AGWs from the source to observation region
837 (e.g. [*Hecht et al.*, 2004b]). The existence of an atmosphere predisposed to forming such

838 a region, due to a temperature inversion, may help to explain this if such inversions
839 are shown to last for many hours. Note that a trapped region formed by a temperature
840 inversion would allow AGWs in all directions to be trapped not just directions determined
841 by large amplitude winds. If the temperature inversion predisposed the atmosphere to
842 form a trapped region even small amplitude wind variations could cause a trapped region
843 to form. While data do show that long-lived temperature inversions, due to planetary
844 waves, can form at mesopause altitudes [*Meriwether and Gerrard, 2004*] it is not known
845 if such inversions form and persist at slightly higher altitudes, above the mesopause.

846 For this event the presence of the quasi two day wave (QTDW) controls the major
847 portion of the wind profile and its long period would be consistent with favorable ducting
848 or trapped conditions existing for many hours. If the existence of a temperature inversion
849 is linked to the presence of planetary waves, and thus the inversions are long-lived, then
850 this might explain the formation of persistent ducts, necessary for the transport of short-
851 wavelength AGWs.

852 In these observations the QTDW may have an effect on the temperature profile. SABER
853 data, at night, over Australia were looked at for several days preceding January 31. A
854 temperature inversion from 80 to 100 km was present around 14 UT on January 31 and 29
855 but was absent at this time on January 30 and 28. The airglow data were also examined
856 for clear periods on those four nights. Brighter and more frequent AGWs occurred on
857 January 29 and January 31 as compared to the nights of January 28 and 30. However, in
858 order to determine if such an association is real more data needs to be examined. Thus,
859 it would be useful to examine the SABER data on a climatological basis to determine the

860 frequency of occurrence of such inversions and whether they are linked to observations of
861 AGWs in imager results.

5. Conclusions

862 The datasets described here (AIRS and airglow images) and obtained on 31 January
863 2006 over central Australia show strong evidence for AGWs that presumably originate in
864 the troposphere, due to processes associated with the large rainfall of an intense tropical
865 low, and then propagate to the stratosphere and to the upper mesosphere. Cloud temper-
866 ature data show that this low formed into a well defined tropical cyclone like cloud field
867 by 31 January 2006, and during the period of 26 to 31 January 2006 there was probably
868 considerable convective as well as stratiform rainfall. Convective rainfall is known to be
869 associated with the formation of AGWs[Vadas *et al.*, 2008]. While after about 12 UT on
870 January 31 stratiform rainfall probably dominated, an additional source for AGWS may
871 be associated with the upper level outflow region of tropical cyclones that are close to
872 inertially neutral.

873 By raytracing the AGWs from the troposphere it is shown that 300/400 km horizontal
874 wavelength 120 minute ground-based period AGWs could be responsible for some of the
875 perturbations seen in the AIRS data at 40 km altitude, and also seen in OHM airglow
876 brightness data over AS near 85 km altitude on 31 January 2006. The AGWs seen in the
877 AIRS data probably originated after 12 UT on 31 January 2006 and thus may be generated
878 by convection or by processes associated with the outflow from cyclones. The AGWs seen
879 in the AS data originated at and before 12 UT and therefore are more probably due to
880 convection.

881 The AS airglow data also show 30 to 45 km horizontal wavelength, 15 to 25 minute
882 ground-based period AGWs being present for many time intervals from 11 to 20 UT on
883 31 January 2006. Raytracing shows those waves could not reach the 80 to 90 km altitude
884 region over AS directly; those waves must have been trapped or ducted. These waves
885 take several hours to reach the mesopause region over AS and they were probably mostly
886 launched before 12 UT on 31 January 2006. Thus, these AGWs were probably generated
887 by convection.

888 The SABER data show that for those short wavelength AGWs a trapped region is almost
889 formed by the temperature profile which shows a temperature inversion. The inclusion
890 of the wind profile obtained from available data and models shows that a trapped region
891 does form. In order for the AGWs to reach AS however, the trapped region must exist for
892 many hours. However, since the winds are dominated by a QTDW, and the temperature
893 profile, from SABER, shows an inversion which extends for many vertical km, such a
894 long-lived region is plausible.

895 The SABER data were also examined to see if inversions were present on previous
896 nights. It was found that an inversion was found on 29 January and 31 January. The AS
897 image data showed that brighter and more frequent waves were seen on those nights. This
898 suggests a connection between the presence of long period waves, such as the QTDW and
899 other planetary waves, and the possibility of trapped AGWs being observed in airglow
900 images over Australia.

901 **Acknowledgments.** Thanks to Peter Strickland and Jeremy Ward for the consider-
902 able help at Alice Springs. Dr. Elizabeth Ebert of the Centre for Australian Weather
903 at the Bureau of Meteorology in Melbourne, Australia provided the rainfall data. The

904 Aerospace Corporation's results could not have been obtained without the invaluable help
905 given by Kirk Crawford in all aspects of this project. JHH, RLW, and LJG were supported
906 by NSF grants ATM-0737557 and ATM-0436516, and by NASA grant NAG5-13025.
907 MJA was supported by the NASA program Earth System Science Research using Data
908 and Products from TERRA, AQUA, and ACRIM Satellites, contracts NNH04CC54C
909 and NNH08AH43I. RAV acknowledges support from Australian Research Council grant
910 DP0558361. The authors acknowledge the SABER science team for their role in develop-
911 ing the scientific algorithms for the SABER temperatures. WRS was supported in part by
912 NASA grant NAG5 5049. PTM acknowledges the support of the Department of Energy
913 Atmospheric Radiation Measurement Program. TWP-ICE was supported under the aus-
914 pices of the US Department of Energy ARM Program, the ARM Uninhabited Aerospace
915 Vehicle (UAV) Program, NASA Cloudsat, the UK Natural Environment Research Council
916 (NERC) Grant Number NE/C512688/1, the NERC Airborne Remote Sensing Facility, the
917 Australian National Marine Research Facility, the Australian Bureau of Meteorology and
918 the Kyoto University Active Geosphere Investigation (KAGI) for the 21st century COE
919 program. Vaisala generously donated the radiosonde base stations. The Charles Darwin
920 University, Darwin RAAF Base and the Tiwi Island Land Council all made extensive
921 facilities available to the experiment.

References

922 Alexander, M. J. and Holton, J. R.: On the spectrum of vertically propagating gravity
923 waves generated by a transient heat source, *Atmos. Chem. Phys.*, 4, 923-932, 2004.

- 924 Alexander, M. J., P. T. May, and J. H. Beres (2004), Gravity waves generated by
925 convection in the Darwin area during DAWEX, *J. Geophys. Res.*, *109*, D20S04,
926 doi:10.1029/2004JD004729.
- 927 Alexander, M.J., and C. Barnet, (2007), Using satellite observations to constrain param-
928 eterizations of gravity wave effects for global models, *J. Atmos. Sci.*, *64*, 1652-1665.
- 929 Alexander, M.J. and H. Teitelbaum, (2007), Observation and analysis of a large ampli-
930 tude mountain wave event over the Antarctic Peninsula, *J. Geophys. Res.*, *112*, D21103,
931 doi:10.1029/2006JD008368.
- 932 Aumann, H. H., et al. (2003), Airs/amsu/hsb on the aqua mission: Design, science objec-
933 tives, data products, and processing systems, *IEEE Trans. Geosci. Remote Sens.*, *41*,
934 253264.
- 935 Dewan, E. M., R. H. Picard, R. R. O'Neill, H. A. Gardiner, J. Gibson, J. D. Mill,
936 E. Richards, M. Kendra, and W. O. Gallery (1998), MSX Satellite Observations of
937 Thunderstorm-Generated Gravity Waves in Mid-Wave Infrared Images of the Upper
938 Stratosphere, *Geophys. Res. Lett.*, *25(7)*, 939-942.
- 939 Eckermann, S. D. and C. J. Marks, An idealized ray model of gravity wave-tidal interac-
940 tions, *J. Geophys. Res.*, *101*, 21195-21212, 1996.
- 941 Ejiri, M. K., K. Shiokawa, T. Ogawa, K. Igarashi, T. Nakamura, and T. Tsuda (2003),
942 Statistical study of short-period gravity waves in OH and OI nightglow images at two
943 separated sites, *J. Geophys. Res.*, *108(D21)*, 4679, doi:10.1029/2002JD002795.
- 944 Fritts, D. C., and M. J. Alexander (2003), Gravity wave dynamics and effects in the
945 middle atmosphere, *Rev. Geophys.*, *41(1)*, 1003, doi:10.1029/2001RG000106.

- 946 Gattinger, R. L., A. V. Jones, J. H. Hecht, D. J. Strickland, and J. Kelly (1991), Com-
947 parison of Ground-Based Optical Observations of N₂ Second Positive to N₂ + First
948 Negative Emission Ratios with Electron Precipitation Energies Inferred from the Son-
949 dre Stromfjord Radar, *J. Geophys. Res.*, *96*(A7), 11,34111,351.
- 950 Gossard, E. E., and W. H. Hooke (1975), *Waves in the atmosphere, atmospheric infra-*
951 *sound and gravity waves - their generation and propagation*, 456pp., Elsevier, Amster-
952 dam.
- 953 Hamilton, K., R. A. Vincent, and P. T. May (2004), The DAWEX field campaign
954 to study gravity wave generation and propagation, *J. Geophys. Res.*, *109*, D20S01,
955 doi:10.1029/2003JD004393.
- 956 Hecht, J. H., R. L. Walterscheid, and M. N. Ross, First measurements of the two-
957 dimensional horizontal wavenumber spectrum from CCD images of the nightglow, *J.*
958 *Geophys. Res.*, *99*, 11,449-11,460, 1994.
- 959 Hecht, J. H., R. L. Walterscheid, D. C. Fritts, J. R. Isler, D. C. Senft, C. S. Gardner, and
960 S. J. Franke (1997), Wave breaking signatures in OH airglow and sodium densities and
961 temperatures 1. Airglow imaging, Na lidar, and MF radar observations, *J. Geophys.*
962 *Res.*, *102*, 6655-6668.
- 963 Hecht, J. H. , R. L. Walterscheid, M. P. Hickey, and S. J. Franke, Climatology and mod-
964 eling of quasi-monochromatic atmospheric gravity waves observed over Urbana Illinois
965 (2001), *J. Geophys. Res.*, *106*(D6), 5181-5196.
- 966 Hecht, J. H. (2004a), Instability layers and airglow imaging, *Rev. Geophys.*, *42*, RG1001,
967 doi:10.1029/2003RG000131.

- 968 Hecht, J. H., S. Kovalam, P. T. May, G. Mills, R. A. Vincent, R. L. Walterscheid, and
969 J. Woithe (2004b), Airglow imager observations of atmospheric gravity waves at Alice
970 Springs and Adelaide, Australia during the Darwin Area Wave Experiment (DAWEX),
971 *J. Geophys. Res.*, *109*, D20S05, doi:10.1029/2004JD004697.
- 972 Hedin, A. E. et al. (1996), Empirical wind model for the upper, middle and lower atmo-
973 sphere, *J. Atmos. Terr. Phy.*, *58*, 1421-1427, doi:10.1016/0021-9169(95)00122-0.
- 974 Holdsworth, D. A., I. M. Reid, and M. A. Cervera (2004), Buckland Park all-sky interfer-
975 ometric meteor radar, *Radio Sci.*, *39*, RS5009, doi:10.1029/2003RS003014.
- 976 Holdsworth, D. A., and I. M. Reid (2004), The Buckland Park MF radar: routine obser-
977 vation scheme and velocity comparisons, *Annales Geophysicae*, *22*(11), 3815-3828.
- 978 Houze, R. A., Jr., *Cloud Dynamics*, 573 pp., Academic Press, San Diego, 1993.
- 979 Jones, W. L., Ray tracing for internal gravity waves, *J. Geophys. Res.*, *74*, 2028-2033,
980 1969.
- 981 Keenan, T.D. and R.E. Carbone (1992), A preliminary morphology of precipitation sys-
982 tems in tropical northern Australia, *Quart. J. Roy. Meteor. Soc.*, *118*, 283-326.
- 983 Killeen, T. L., W. R. Skinner, R. M. Johnson, C. J. Edmonson, Q. Wu, R. J. Niciejewski,
984 H. J. Grassl, D. A. Gell, P. E. Hansen, J. D. Harvey, and J. F. Kafkalidis, TIMED
985 Doppler Interferometer (TIDI) in *SPIE Conference on Optical Spectroscopic Techniques*
986 *and Instrumentation for Atmospheric and Space Research III*, *SPIE 3756*, pp. 289-301,
987 Denver, Colorado, 1999.
- 988 Larsen, M. F. (2002), Winds and shears in the mesosphere and lower thermosphere:
989 Results from four decades of chemical release wind measurements, *J. Geophys. Res.*,
990 *107*(A8), 1215, doi:10.1029/2001JA000218.

- 991 Lighthill, J., *Waves in fluids*, 504pp., (2001 reprint), Cambridge University Press, Cam-
992 bridge, 1978.
- 993 Marks, C. J., and S. D. Eckermann, A three-dimensional nonhydrodynamic ray-tracing
994 model for gravity waves: Formulation and preliminary results for the middle atmo-
995 sphere, *J. Atmos Sci.*, *52*, 1959-1984, 1995.
- 996 May P.T., G.J. Holland and W.L. Ecklund (1994), Wind profiler observations of tropical
997 storm Flo at Saipan, *Wea. Forecast.*, *9*, 410-426.
- 998 May, P. T, J. H. Mather, G. Vaughan, C. Jakob, G. M. McFarquhar, K. N. Bower, and
999 G. G. Mace (2008), The Tropical Warm Pool International Cloud Experiment, *Bulletin*
1000 *of the American Meteorological Society*, *89*, 629-645, doi:10.1175/BAMS-89-5-629.
- 1001 Meriwether J. W., A. J. Gerrard (2004), Mesosphere inversion layers and stratosphere
1002 temperature enhancements, *Rev. Geophys.*, *42*, RG3003, doi:10.1029/2003RG000133.
- 1003 Mertens, C. J., M. G. Mlynczak, M. Lopez-Puertas, P. P. Wintersteiner, R. H. Picard, J.
1004 R. Winick, L. L. Gordley, and J. M. Russell III (2001), Retrieval of mesospheric and
1005 lower thermospheric kinetic temperature from measurements of CO₂ 15 μ m Earth limb
1006 emission under non-LTE conditions, *Geophys. Res. Lett.*, *28*(7), 1391-1394.
- 1007 Nakamura, T., A. Higashikawa, T. Tsuda, and Y. Matsushita (1999), Seasonal variations
1008 of gravity wave structures in OH airglow with a CCD imager at Shigaraki, *Earth,*
1009 *Planets, and Space*, *51*, 897-906.
- 1010 Nakamura, T., T. Aono, T. Tsuda, A. G. Admiranto, E. Achmad, and Suranto (2003),
1011 Mesospheric gravity waves over a tropical convective region observed by OH airglow
1012 imaging in Indonesia, *Geophys. Res. Lett.*, *30*(17), 1882, doi:10.1029/2003GL017619.

- 1013 Niciejewski, R., Q. Wu, W. Skinner, D. Gell, M. Cooper, A. Marshall, T. Killeen, S.
1014 Solomon, and D. Ortland (2006), TIMED Doppler Interferometer on the Thermosphere
1015 Ionosphere Mesosphere Energetics and Dynamics satellite: Data product overview, *J.*
1016 *Geophys. Res.*, *111*, A11S90, doi:10.1029/2005JA011513.
- 1017 Pautet, P.-D., M. J. Taylor, A. Z. Liu, and G. R. Swenson (2005), Climatology of short-
1018 period gravity waves observed over northern Australia during the Darwin Area Wave Ex-
1019 periment (DAWEX) and their dominant source regions, *J. Geophys. Res.*, *110*, D03S90,
1020 doi:10.1029/2004JD004954.
- 1021 Press, W. H., S. A. Teukolsky, W. T. Vettering, and B. P. Flannery, *Numerical Recipes*
1022 *The Art of Scientific Computing Second Edition*, 1020pp, Cambridge University Press,
1023 Cambridge, 1993.
- 1024 P. Preusse, S. D. Eckermann, J. Oberheide, M. E. Hagan, D. Offermann, Modulation of
1025 gravity waves by tides as seen in CRISTA temperatures, *Advances in Space Research*,
1026 *Volume 27*, Issue 10, 2001, Pages 1773-1778, ISSN 0273-1177, DOI: 10.1016/S0273-
1027 1177(01)00336-2.
- 1028 Remsberg E. E., et al. (2008), Assessment of the quality of the Version 1.07 temperature-
1029 versus-pressure profiles of the middle atmosphere from TIMED/SABER, *J. Geophys.*
1030 *Res.*, *113*, D17101, doi:10.1029/2008JD010013.
- 1031 Russell, J. M., III, M. G. Mlynczak, L. L. Gordley, J. Tansock, An overview of the SABER
1032 experiment and preliminary calibration results, *Proceedings of the SPIE, 44th Annual*
1033 *Meeting*, Denver, Colorado, July 18-23, vol. 3756, pp. 277-288,1999.
- 1034 Schubert, G., R. L. Walterscheid, and M. P. Hickey (1991), Gravity Wave-Driven Fluctu-
1035 ations in OH Nightglow From an Extended, Dissipative Emission Region, *J. Geophys.*

- 1036 *Res.*, *96(A8)*, 13,86913,880.
- 1037 Sentman, D.D., Wescott, E.M., Picard, R.H., Winick, J.R., Stenbaek-Nielsen, H.C., De-
1038 wan, E.M., Moudry, D.R., Sao Sabbas, F.T., Heavner, M.J. and Morrill, J., (2003).
1039 Simultaneous observations of mesospheric gravity waves and sprites generated by a
1040 midwestern thunderstorm, *J. Atmos. Solar Terres. Phys.* *65*, 537-550.
- 1041 Skinner, W. R., R. J. Niciejewski, T. L. Killeen, S. C. Solomon, D. Gablehouse, Q. Wu,
1042 D. Ortland, D. A. Gell, A. R. Marshall, E. Wolfe Jr., M. Cooper, J. F. Kafkalidis, Op-
1043 eration performance of the TIMED Doppler Interferometer (TIDI) in *SPIE Conference*
1044 *on Optical Spectroscopic Techniques and Instrumentation for Atmospheric and Space*
1045 *Research V, SPIE 5157*, edited by Allen M. Larar, Joseph A. Shaw, and Zhaobo Sun,
1046 pp. 47-57, San Diego, Ca., 2003.
- 1047 Snively, J. B., and V. P. Pasko (2008), Excitation of ducted gravity waves in
1048 the lower thermosphere by tropospheric sources, *J. Geophys. Res.*, *113*, A06303,
1049 doi:10.1029/2007JA012693
- 1050 Suzuki, S., K. Shiokawa, Y. Otsuka, T. Ogawa, and P. Wilkinson (2004), Statistical
1051 characteristics of gravity waves observed by an all-sky imager at Darwin, Australia, *J.*
1052 *Geophys. Res.*, *109*, D20S07, doi:10.1029/2003JD004336.
- 1053 Swinbank, R. and D. A. Ortland, Compilation of wind data for the UARS reference
1054 atmosphere project, *J. Geophys. Res.*, *108*, 4615, doi:10.1029/2002JD003135, 2003.
- 1055 Taylor, M. J., and M. A. Hapgood, M. A. (1988), Identification of a thunderstorm as
1056 a source of short period gravity waves in the upper atmospheric nightglow emissions.
1057 *Planet. Space Sc.*, *36*, 975-985.

- 1058 Torrance, C. T. and G.P. Compo (1998), A practical guide to wavelet analysis, *Bull.*
1059 *Amer. Meteor. Soc.*, *71*, 61-78.
- 1060 Vadas, S.L. and D. C. Fritts (2006), Thermospheric responses to gravity waves: Influ-
1061 ences of increasing viscosity and thermal diffusivity, *J. Geophys. Res.*, *110*, D15103,
1062 doi:10.1029/2004JD005574.
- 1063 Vadas, S., M. J. Taylor, D. Pautet, P. A. Stamus, D. C. Fritts, F. Sao Sabbas, and V. Thi-
1064 ago (2008), Convection: the Likely Source of the Medium-Scale Gravity Waves Observed
1065 in the OH Airglow Layer near Brasilia, Brazil, During the SpreadFEx Campaign, *Ann.*
1066 *Geophys.*, submitted..
- 1067 Walterscheid, R. L., J. H. Hecht, R. A. Vincent, I. M. Reid, J. Woithe, and M. P.
1068 Hickey, Analysis and Interpretation of Airglow and Radar Observations of Quasi-
1069 Monochromatic Gravity Waves in the Upper Mesosphere and Lower Thermosphere over
1070 Adelaide, Australia (35 S, 138 E), *J. Atmos. Solar-Terr. Phys.* , *61*, 461-468, 1999.
- 1071 Walterscheid, R. L., G. Schubert, and D. G. Brinkman, Small-scale gravity waves in the
1072 upper mesosphere and lower thermosphere generated by deep tropical convection, *J.*
1073 *Geophys. Res.*, *106*(D23), 31825-31832, 10.1029/2000JD000131, 2001.
- 1074 Walterscheid, R. L., and J. H. Hecht (2003), A reexamination of evanescent acoustic-
1075 gravity waves: Special properties and aeronomical significance, *J. Geophys. Res.*,
1076 *108*(D11), 4340, doi:10.1029/2002JD002421.

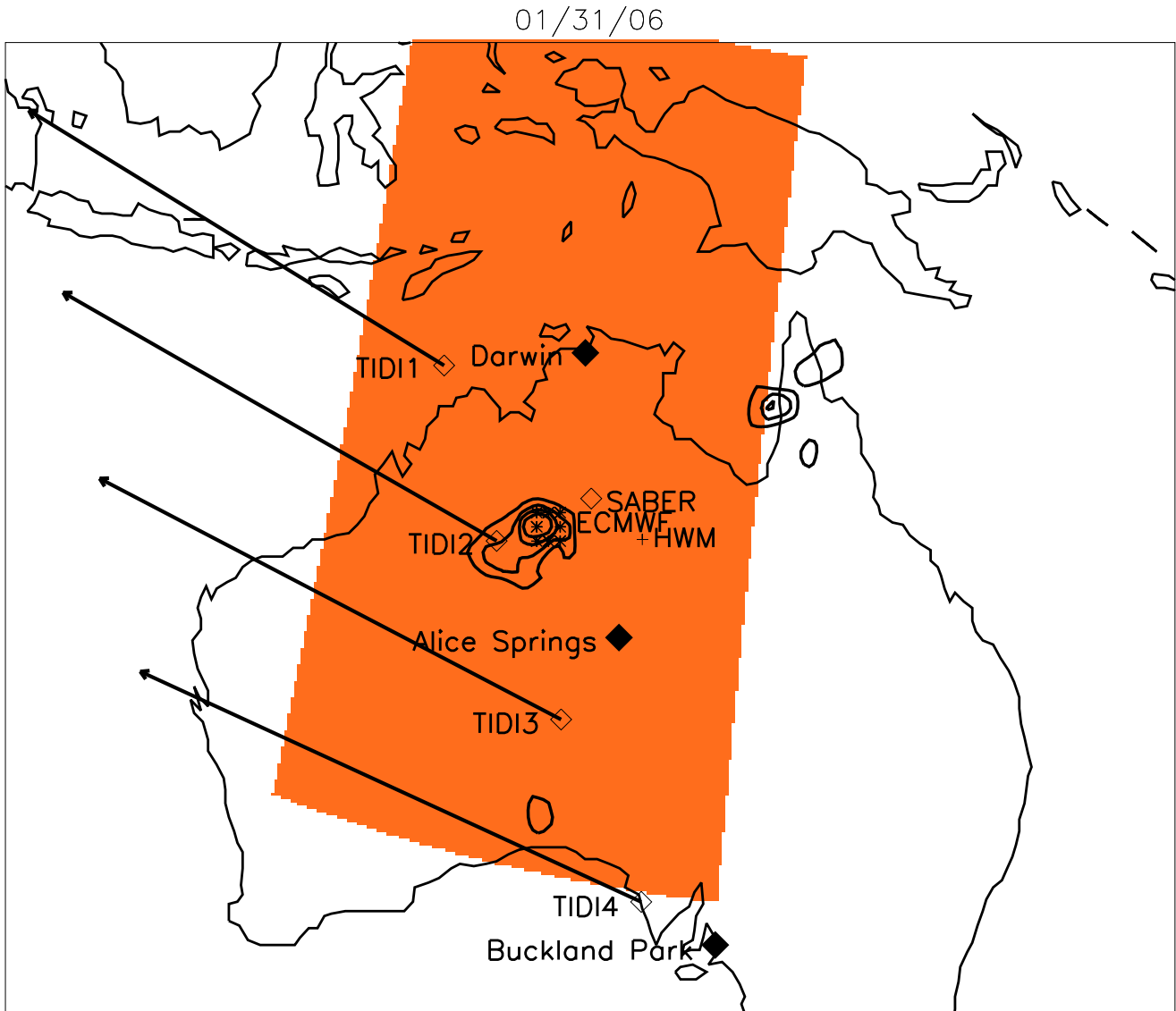


Figure 1. Map of Australia showing the locations of the instruments and models used in this work. The orange represents the extent of the AIRS data swath. The solid diamonds are ground-based sites. The hollow diamonds are the tangent points of the AIRS and TIMED (TIDI and SABER) satellite observations. The satellite is located off the west coast of Australia moving north to south. Lines are shown from the TIDI tangent points to the satellite location, shown at the end of the arrowhead. The stars enclose the ECMWF grid point. The plus sign shows the location of the HWM profile. See also Table 1. The major rainfall contours over Australia are also shown (see Figure 9).

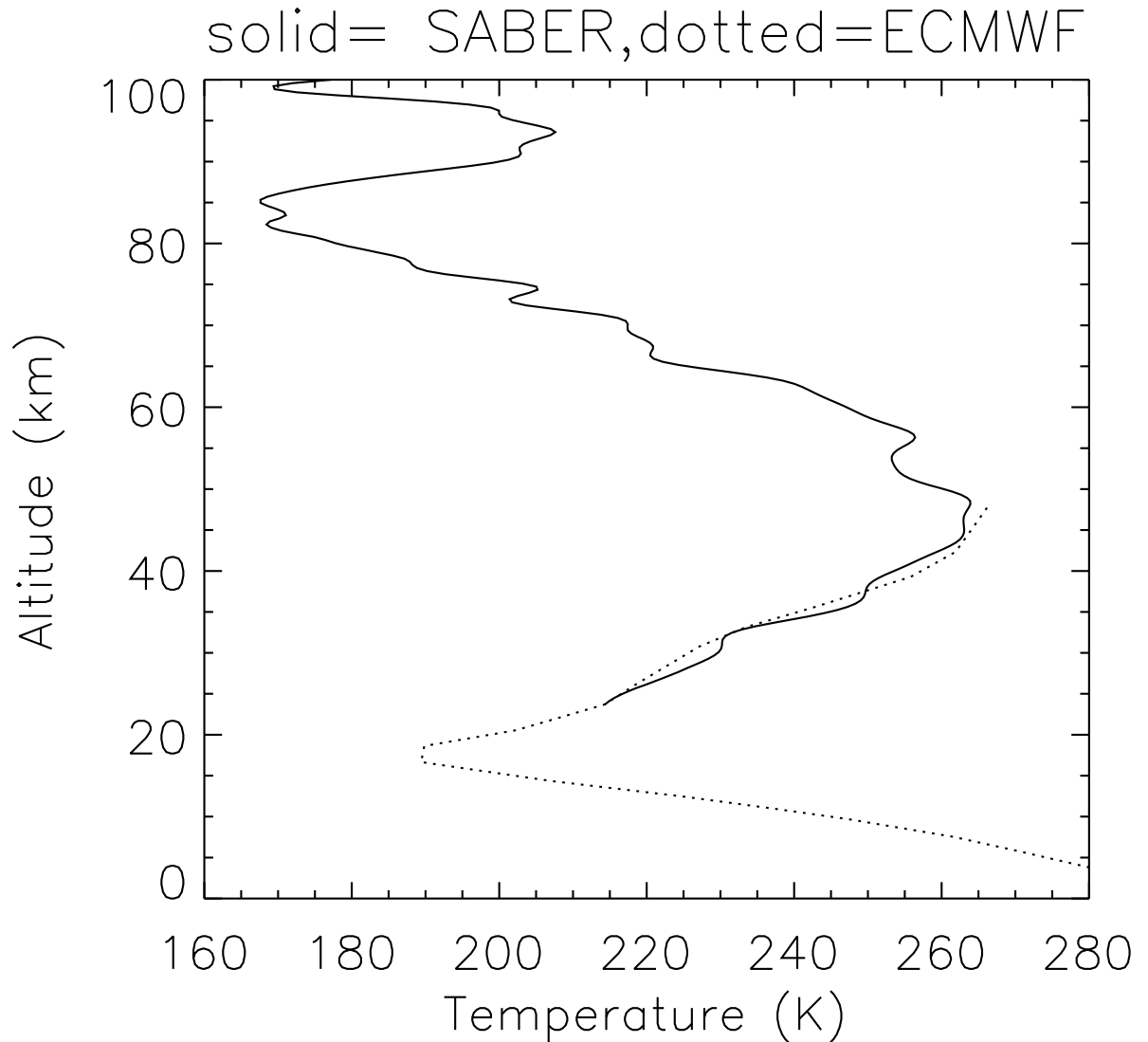


Figure 2. Plot of the adopted temperature profile from SABER (solid) and the ECMWF (dotted) results. The SABER profile is taken from the overpass on 31 January 2006 at 1414 UT and has a tangent altitude at approximately 18.38° south latitude and 132.55° east longitude. The ECMWF analysis was for 12 UT at approximately 19.5° south latitude and 130.5° east longitude close to the center of the rainfall seen in Figure 8.

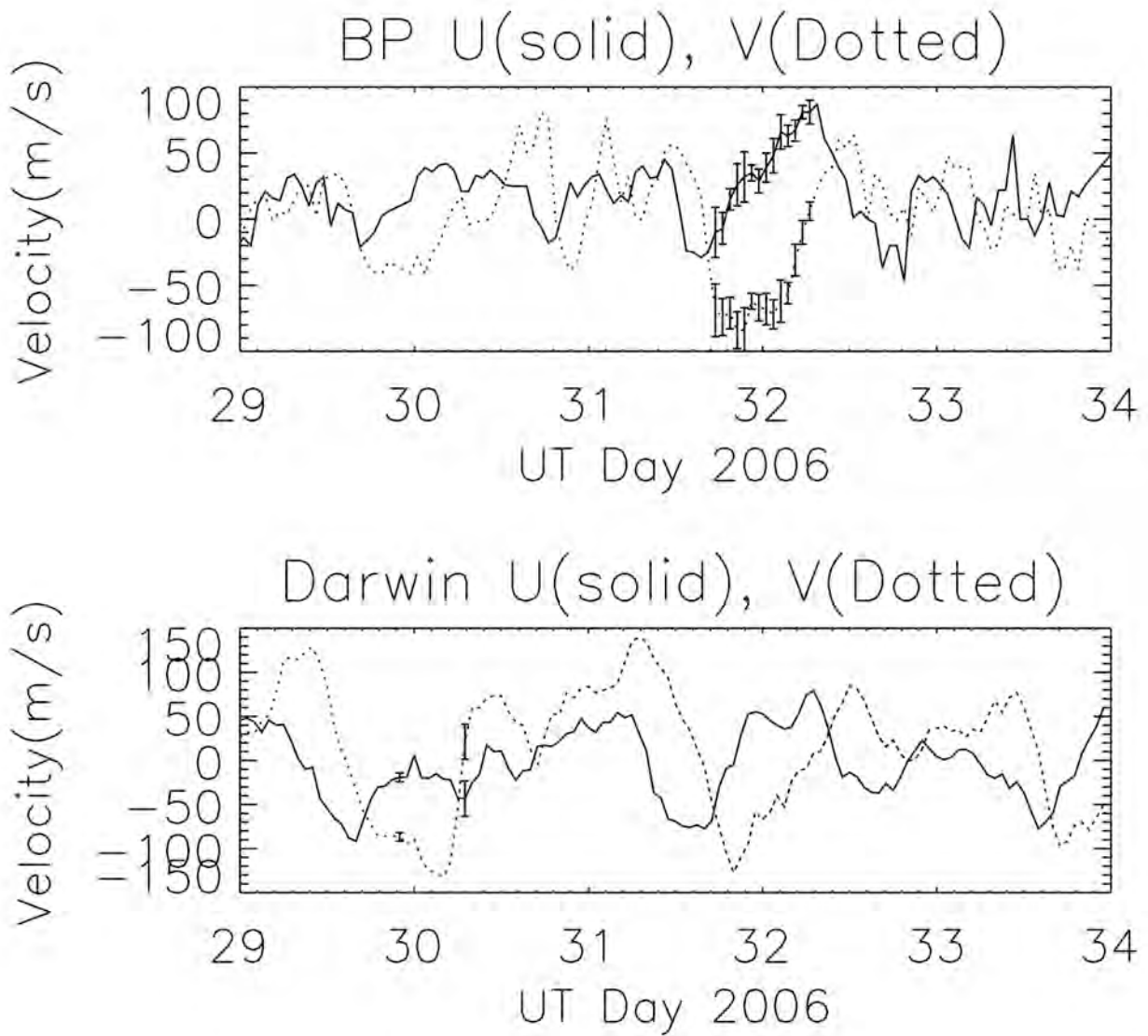


Figure 3. Top-Plots of U (solid) and V (dotted) components at 88 km altitude from MF radar data at Buckland Park for days 29-33 of 2006. Bottom-same but from meteor radar at Darwin. Representative error bars are shown.

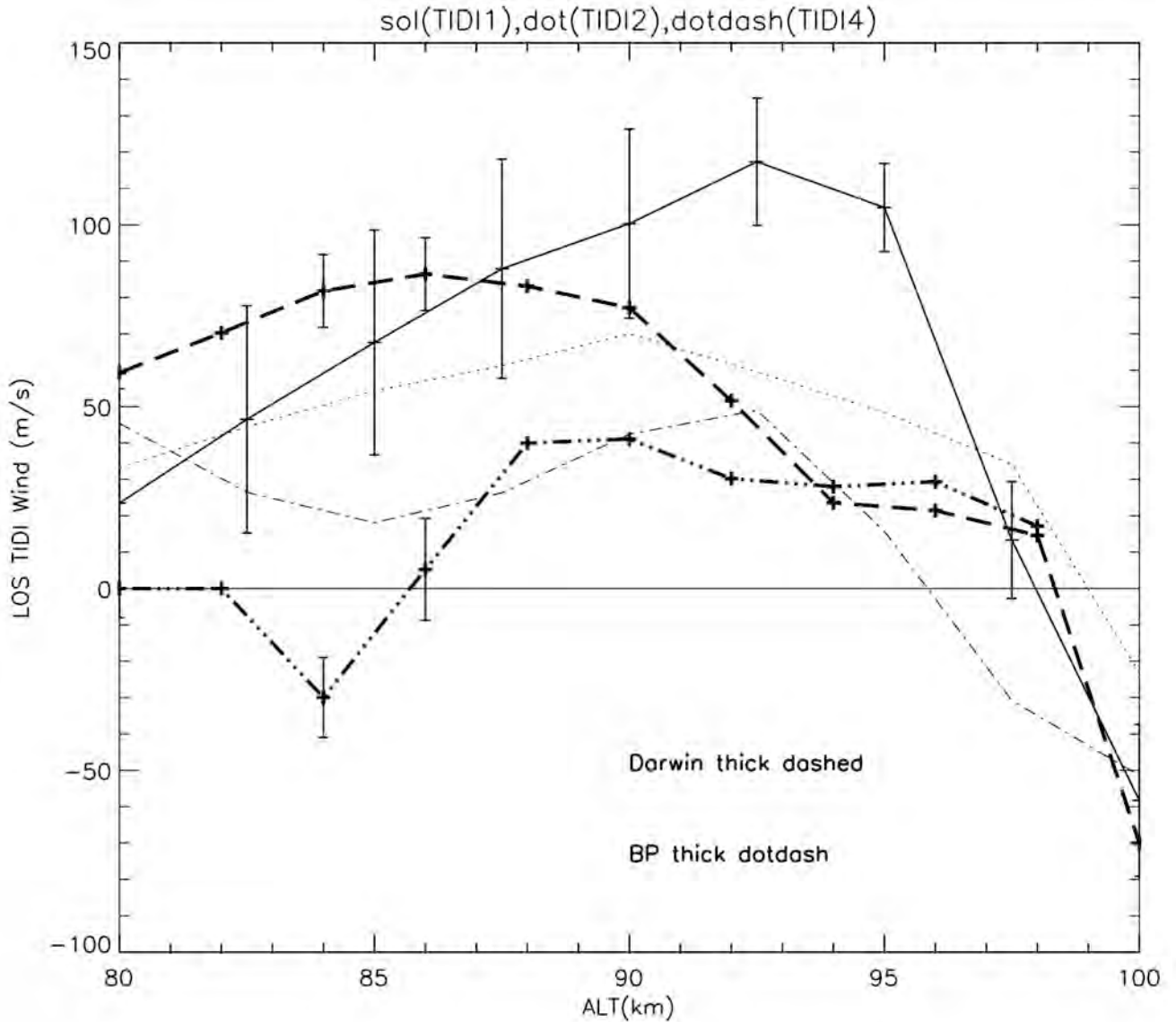


Figure 4. Plot of the LOS (approximately 116 degrees E of N) winds from TIDI at about 1415 UT on 31 January 2006 at 3 positions over central Australia. These positions, TIDI1(13S,125E), TIDI2(20S,128E) and TIDI4(33S,135E), are shown in Figure 1. Also shown are the winds from the BP(35S,139E) and Darwin(12.5S,131E) radars at 14 UT. A reference line is shown at 0 m/s. Error bars are shown for the TIDI1 plot. The other TIDI errors are similar. For the radar data representative error bars are shown for two altitudes (84 and 86 km).

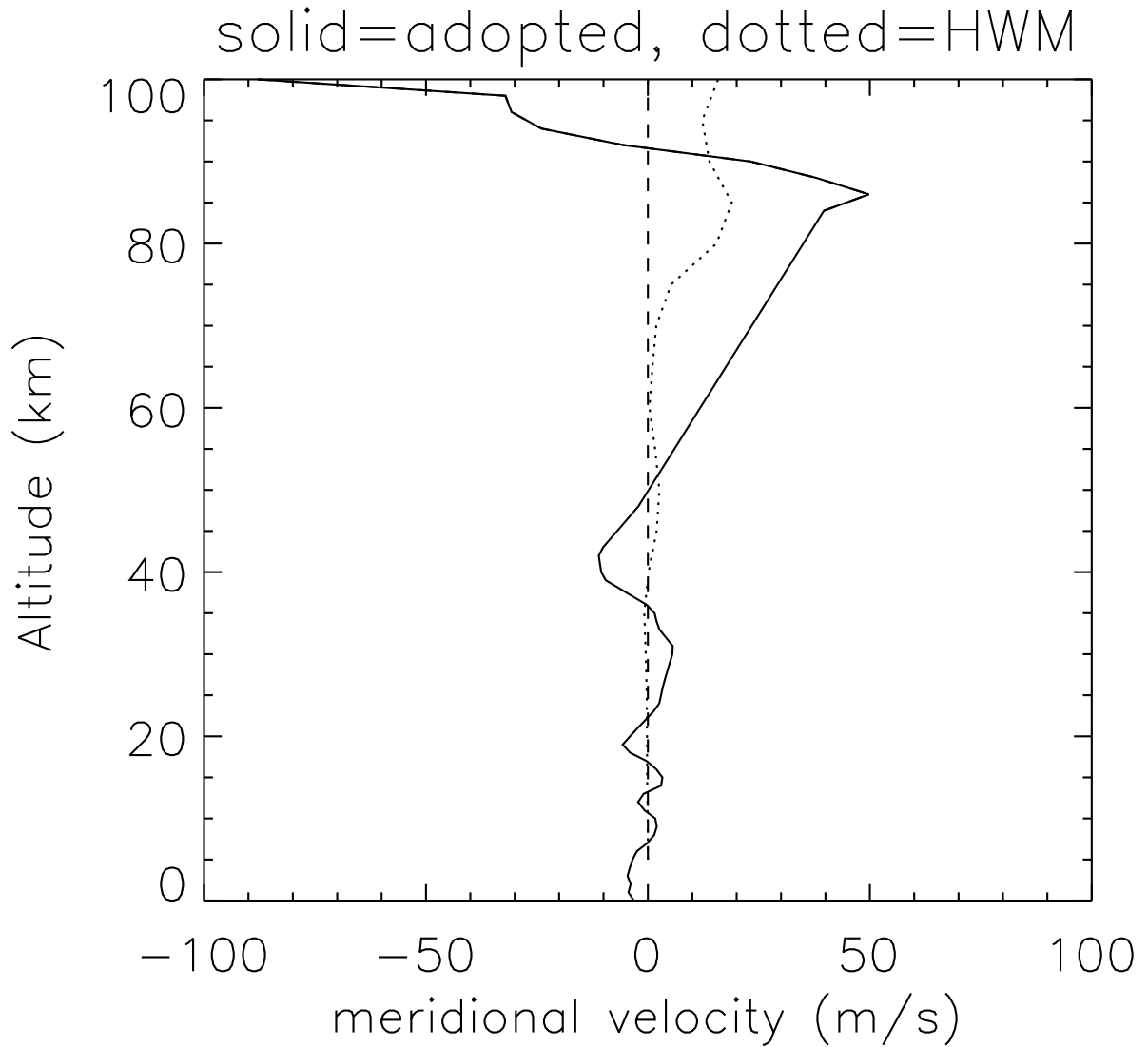


Figure 5. Plot of the adopted meridional profile (solid) and the closest HWM result at 20S, 135E (dotted). The dashed line shows 0 m/s velocity to guide the reader.

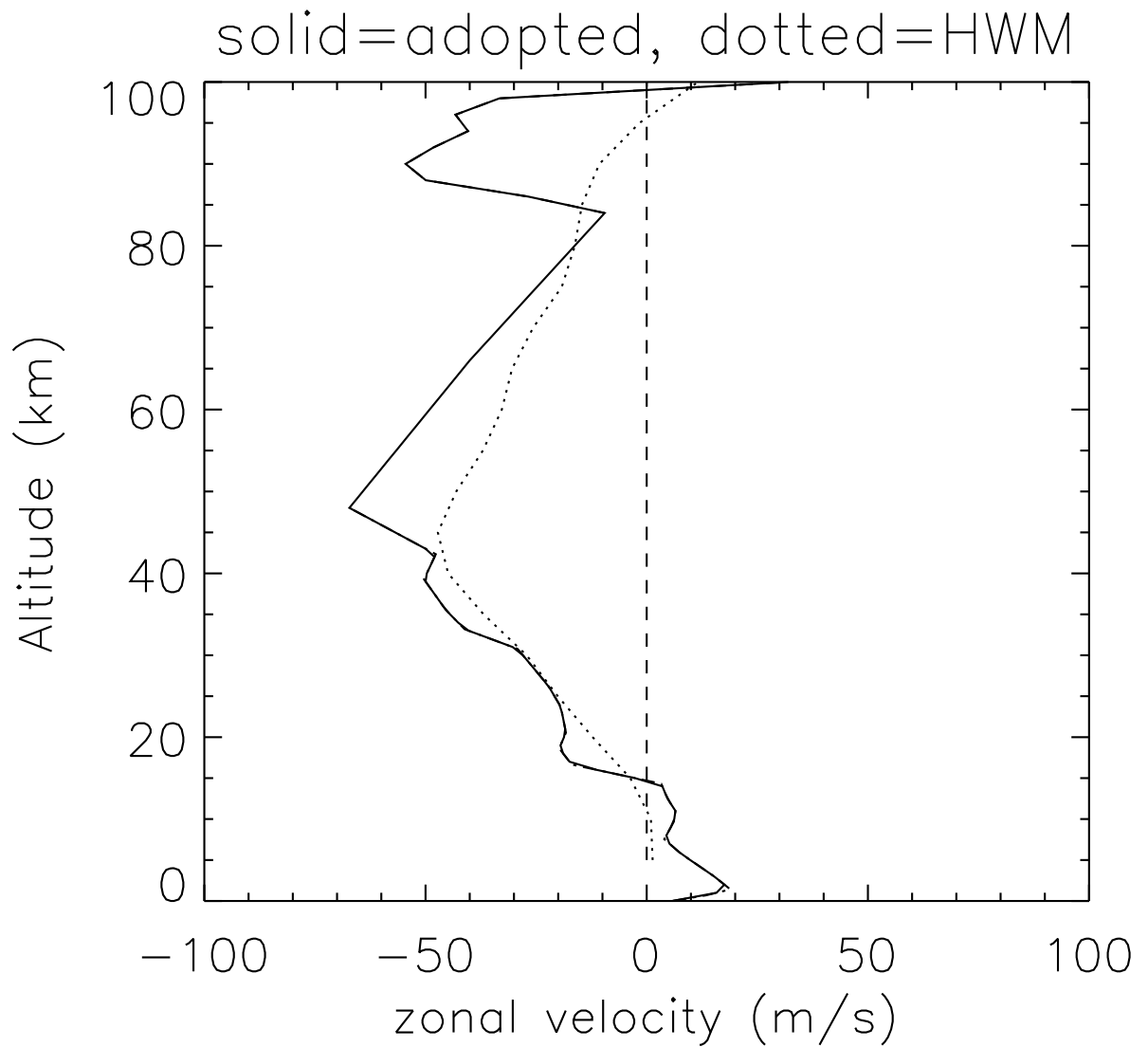


Figure 6. Plot of the adopted zonal profile (solid) and the closest HWM result at 20S, 135E (dotted). The dashed line shows 0 m/s velocity to guide the reader.

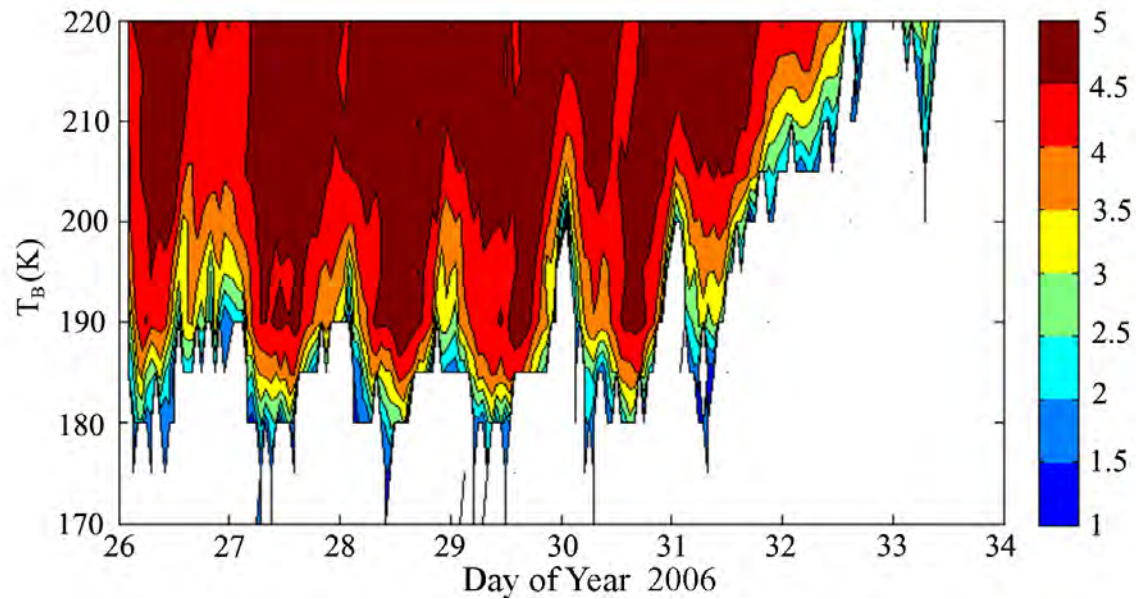


Figure 7. Shows contours, in intervals of 0.5, of the \log_{10} of the area in km^2 (between 15° to 23° south latitude and 125° to 135° east longitude) covered by cloud top IR brightness temperatures (T_B) as a function of time. Tickmarks correspond to 00 UT of the day of the year in 2006. The plotted T_B values includes data from plus or minus 2.5 K from the nominal T_B .

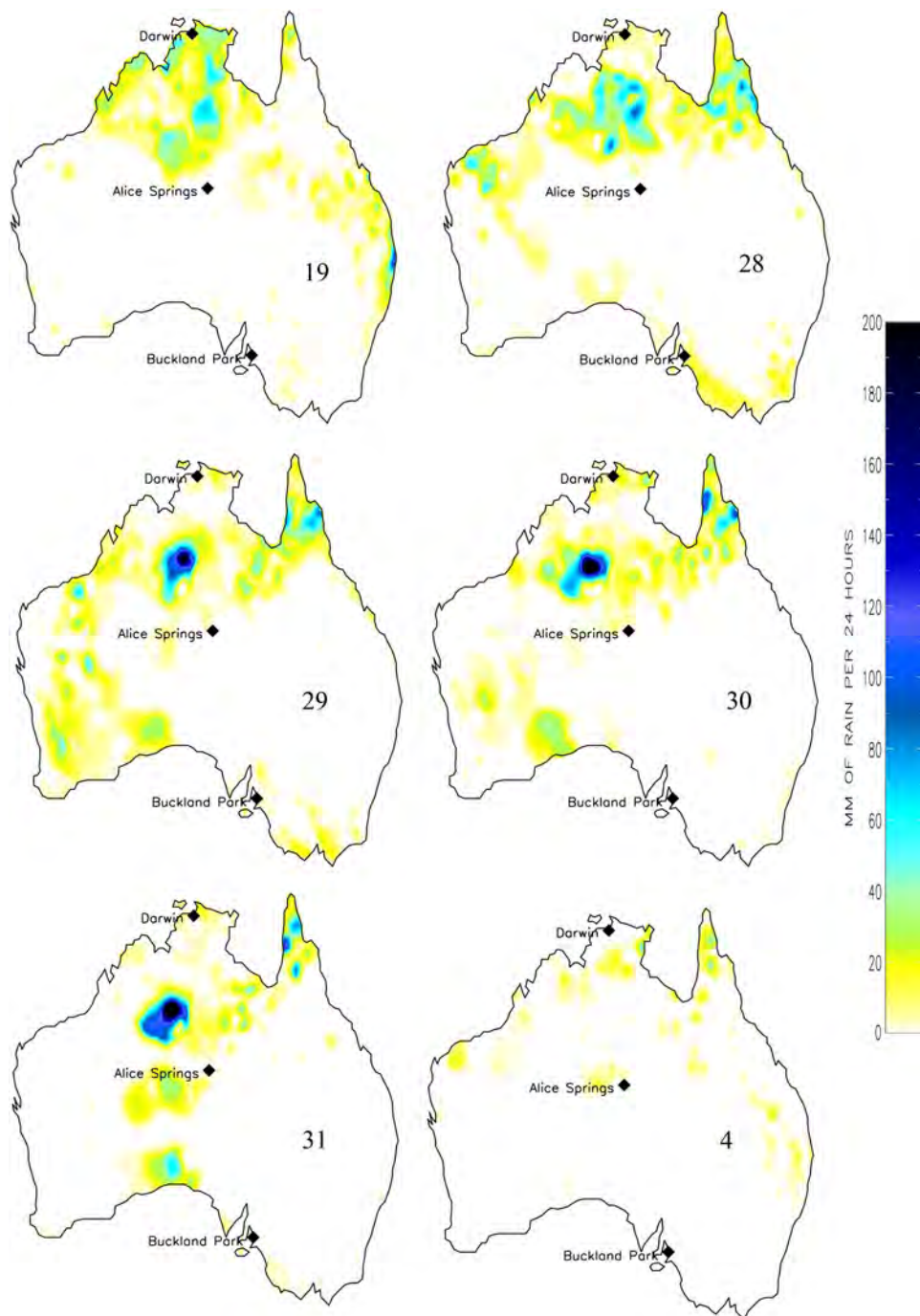


Figure 8. Rainfall maps over Australia (mm of rain per 24 hours) for January days 19 (upper left), 28-31 and February 4 (lower right) of 2006

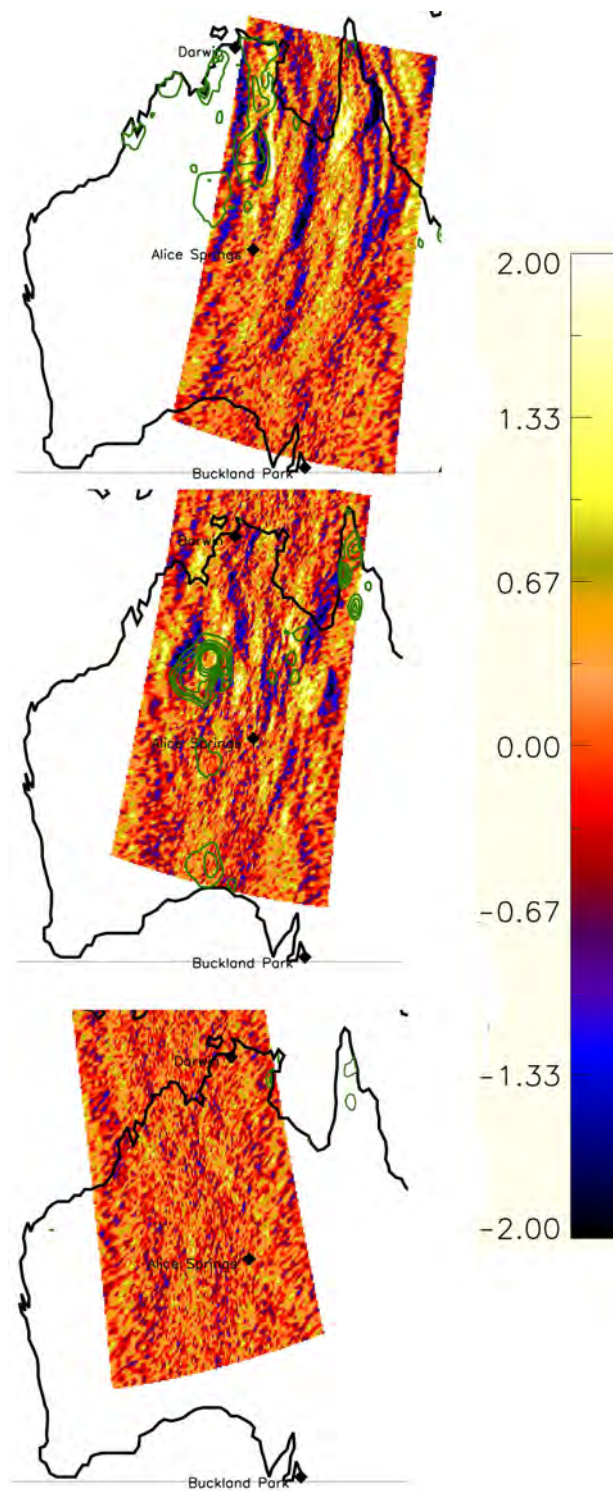


Figure 9. Images of radiance perturbations ($\text{mW}/\text{m}^2\text{-sr-cm}^{-1}$) from the mean calculated from AIRS data originating near 40 km altitude. The contours represent rainfall amounts as shown in Figure 8. The first contour represents 25 mm of rainfall over 24 hours. (Top) 1559 UT on 19 January 2006. (Middle) 1623 UT on 31 January 2006. (Bottom) 0505 UT on 4 February 2006

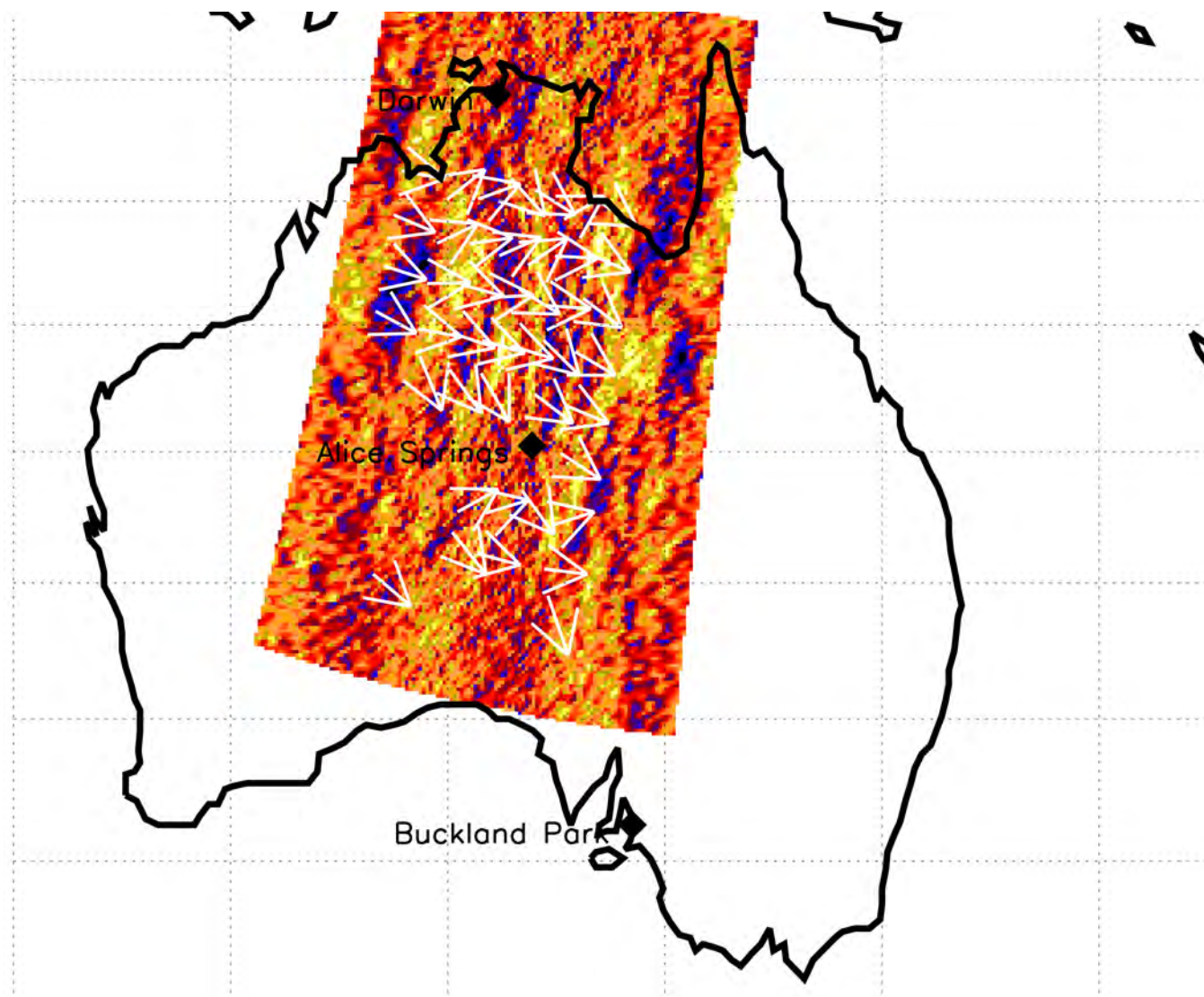


Figure 10. Same as middle panel of Figure 9. without any rainfall contours, but also showing the directionality of the dominant wave from the wavelet analysis.

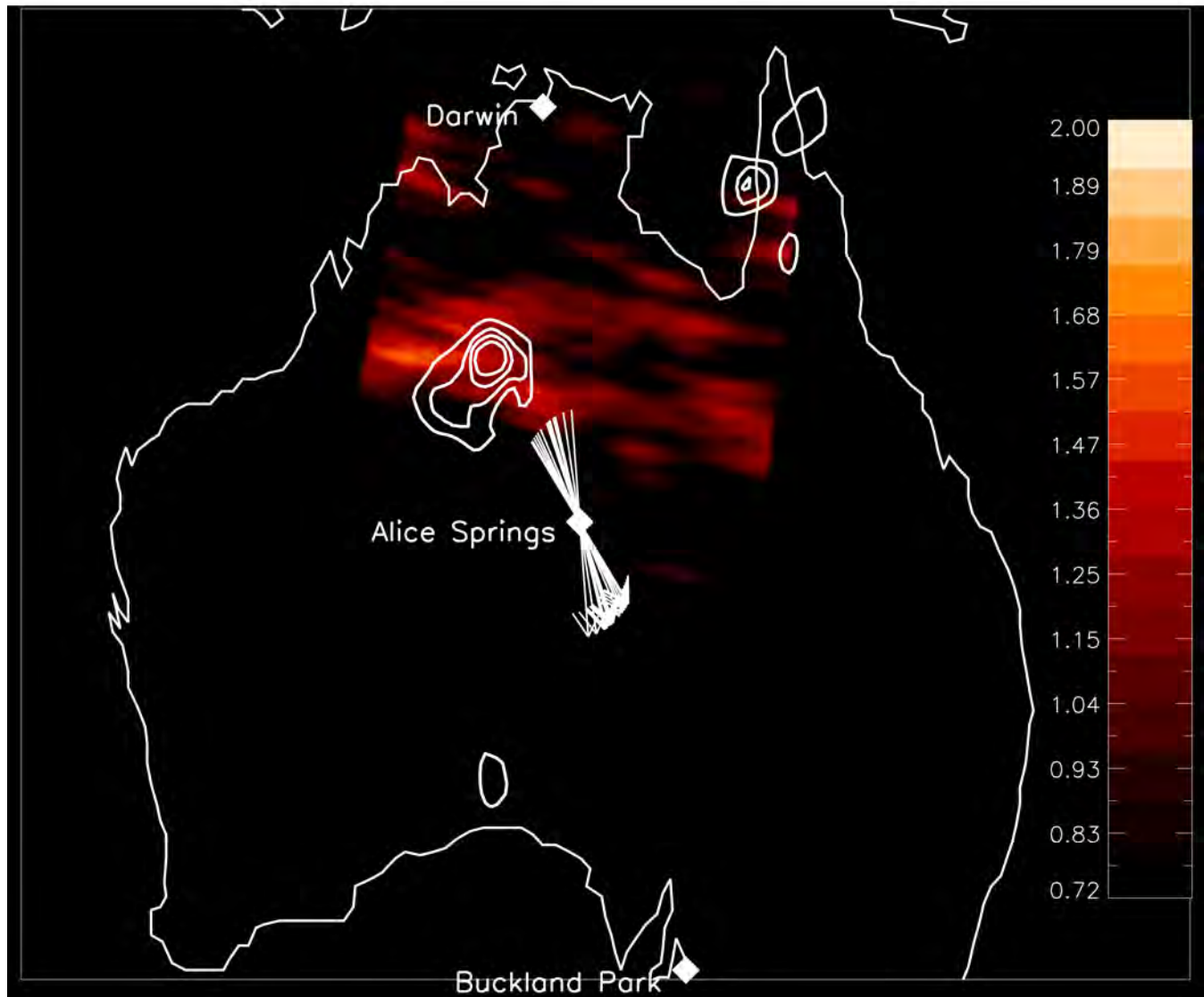


Figure 11. Plots of wave amplitudes ($\text{mW}/\text{m}^2\text{-sr}\cdot\text{cm}^{-1}$) from the wavelet analysis on the middle panel of Figure 9. The amplitudes have a threshold of 0.72 which represents approximately a signal three times the noise. The white arrows show the directionality small horizontal wavelength AGWs observed by the Alice Springs imager. Here the first contour represents 50 mm of rainfall over 24 hours.

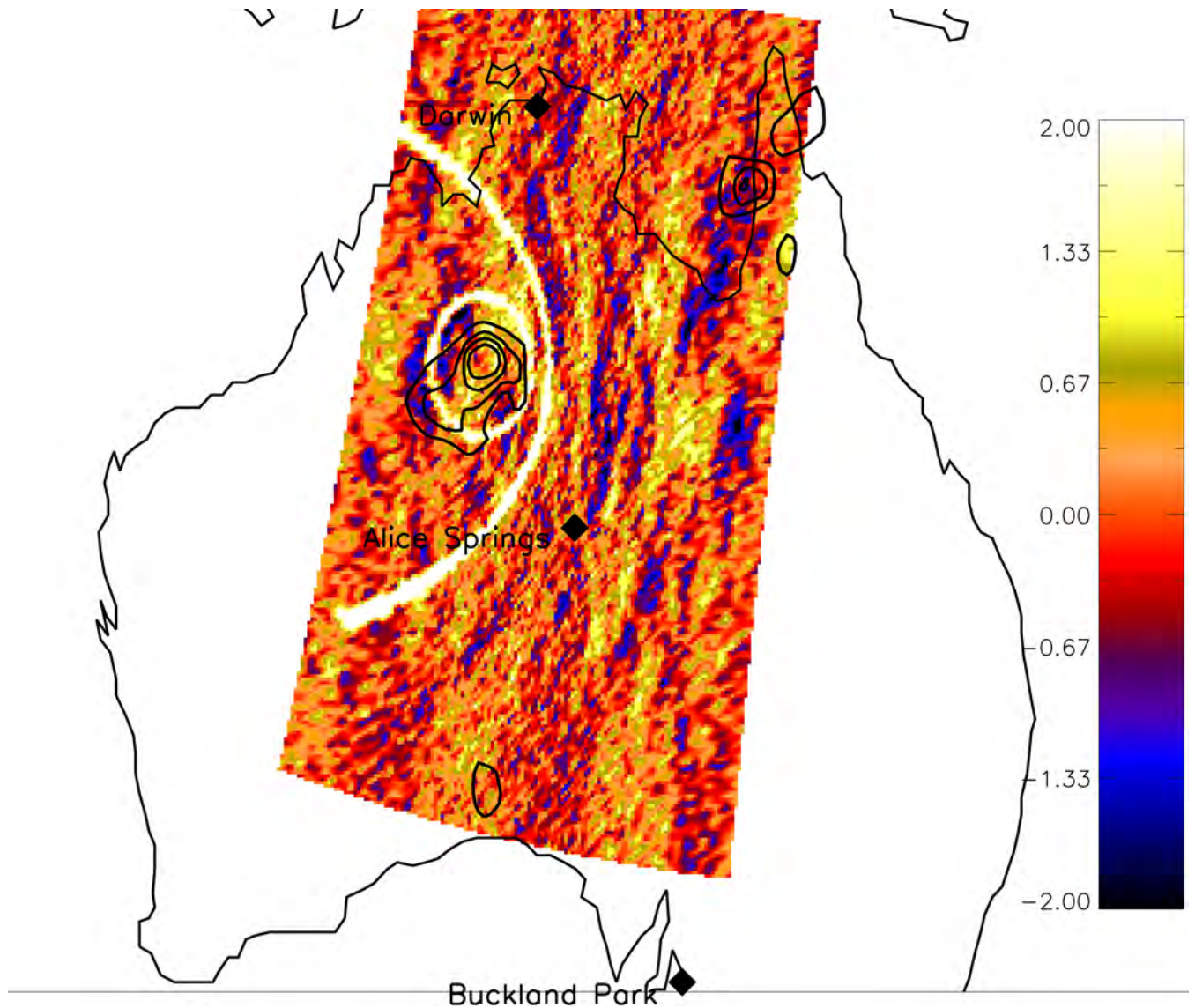


Figure 12. Same as middle panel of Figure 9 but also showing the position of a $300 \text{ km } \lambda_h$ 120 minute ground-based period wave (outer partial circle) when it reaches 40 km altitude. For clarity in this plot the circle is only drawn where the distance to the center of the storm is less than 600 km. The inner complete circle is for the position of a $300 \text{ km } \lambda_h$ 25 minute ground-based period wave when it reaches 40 km altitude. Here the first contour represents 50 mm of rainfall over 24 hours.

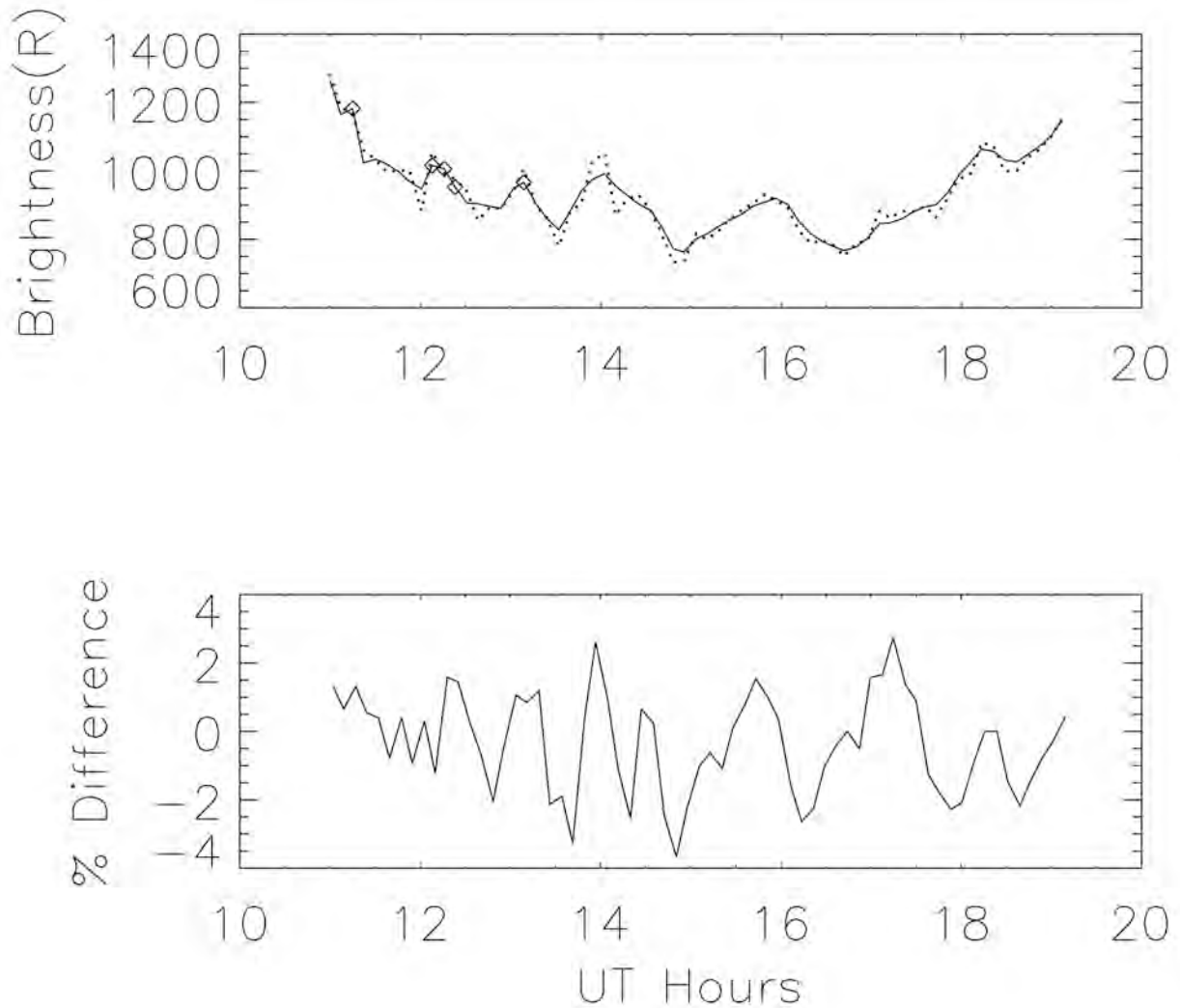


Figure 13. Top-OH brightness, in Rayleighs, measured by AS imager on 31 January 2006. The solid line is the average over approximately an 58 x 90 km box while the dotted line is an average over a 10 x 16 km box. The diamonds indicates images where there were clouds obscuring individual stars. Bottom-A plot of the percent difference between the lines in the top panel. The statistical uncertainties are less than one percent of the brightness values.

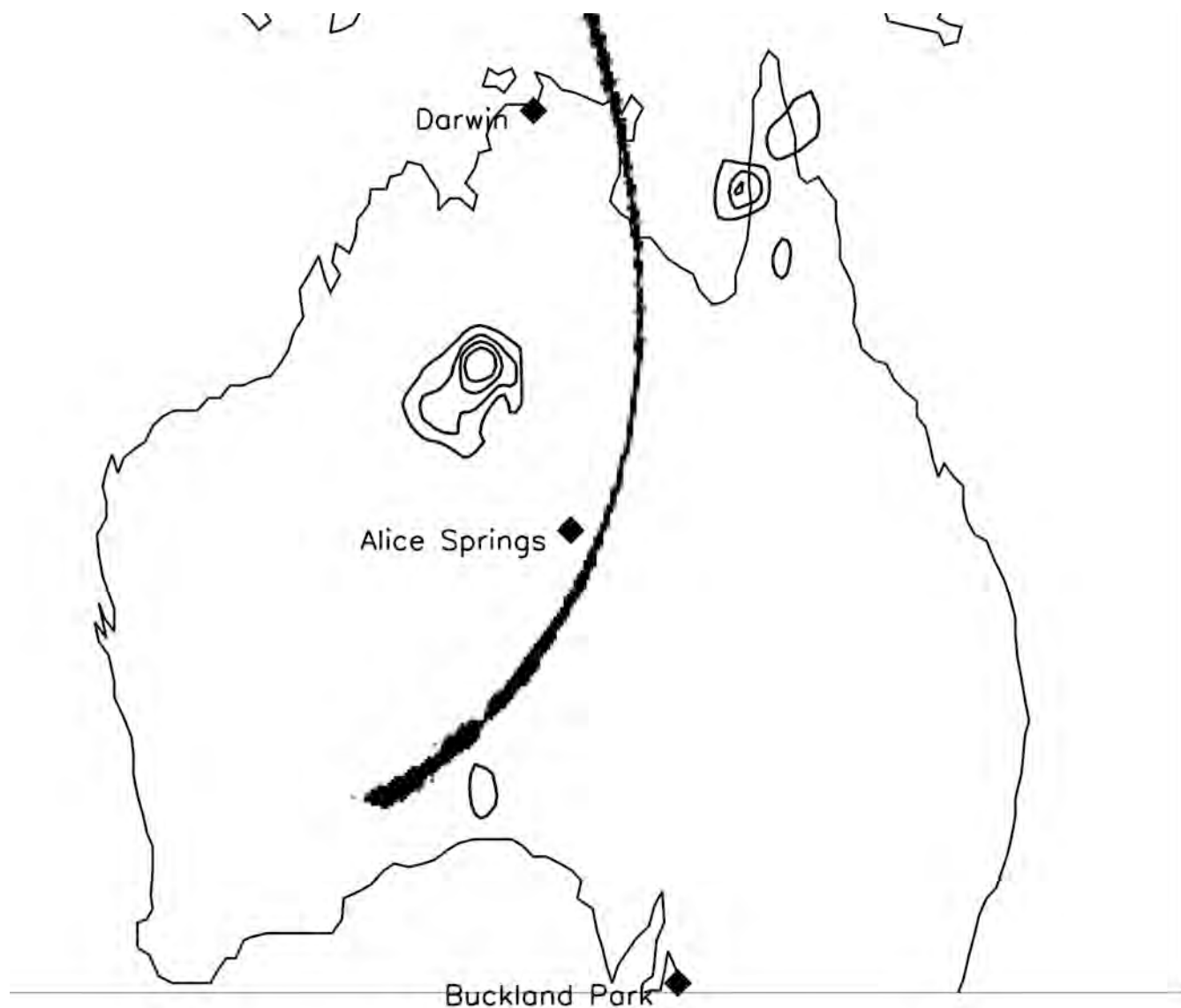


Figure 14. Similar to Figure 12 but showing a partial circle indicating the position, as determined by a raytrace, of a 400 km λ_h 120 minute ground-based period AGW when it reaches 80 km altitude. For clarity as in Figure 11 only part of the circle is shown.

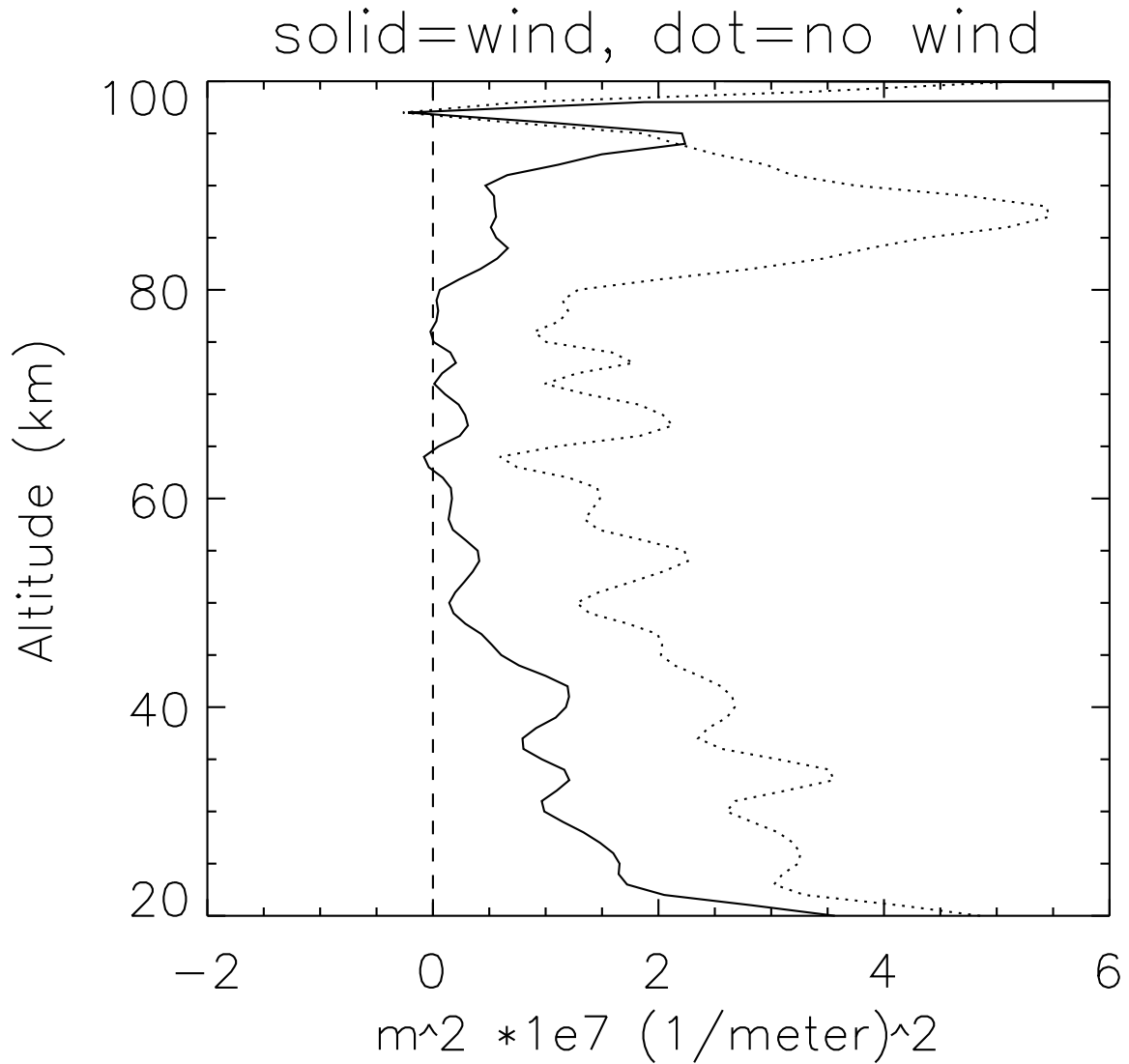


Figure 15. Plot of m^2 from the dispersion relation for an AGW launched at an azimuth of 150 degrees east of north with a λ_h of 35 km and a ground-based period of 15 minutes. With winds (solid), without winds (dotted). The evanescent regions, where m^2 are less than zero, are present for λ_h values up to about 45 km for ground-based periods of 15 minutes. At a λ_h of 30 km the evanescent region remains until ground-based periods reach around 25 minutes.

Table 1. Data Sources

Technique	Type	Location	Lat(Lon)	Time(UT)	Parameter	Altitude(km)	Results
GB	Imager	AS	23.8(133.9)	10-19	Images(OH)	85	AGW λ_h and
SAT	AIRS	Aqua	Fig 1	16.4	IR(CO ₂)	40	AGW λ_h
GB	Meteor radar	DR	12.5(130.8)	Hourly	W	80-100	W 80 -100 km
GB	MF radar	BP	34.9(138.6)	Hourly	W	80-100	W 80 -98 km
SAT	SABER	TIMED	18.38(132.55)	14.2	T	15-100	T 15-100 km
SAT	TIDI	TIMED	(Fig 1)	14.2	W	80-100	see 2.2.2
A	ECMWF	NA	19.5(130.5)	12	W/T	15-50	W/T 15-50
M	HWM/URAP	NA	20(135)	12	W/T	50-84	see 2.2.2

GB=Ground-Based,SAT=Satellite,A=Assimilation,M=Model,

AS=Alice Springs,DR=Darwin,W=Wind,T=Temperature